Engineering Geology 363 (2026) 108559

Contents lists available at ScienceDirect

Engineering Geology

journal homepage: www.elsevier.com/locate/enggeo

Seismic analysis of a zoned earth dam after decades of operation

Mariagrazia Tretola [a], Lucia Coppola [b], Stefania Sica [a,*], Luca Pagano [b]

[a] Department of Engineering, University of Sannio, P.za Roma 21, 82100 Benevento, Italy
[b] Department DICEA, University of Napoli Federico II, Via Claudio 21, Napoli, Italy

ARTICLE INFO

Keywords:
Zoned earth dam
Earthquake
Monitoring
Dynamic analysis

ABSTRACT

The seismic safety assessment of zoned earth dams that have been in operation for several decades requires a preliminary evaluation of their pre-seismic behavior through the interpretation of monitoring data and laboratory tests on construction materials, collected throughout the dam's service life. Once it is verified whether any factors have influenced the dam's performance and whether this behavior remains consistent with the original design expectations, the seismic response can be analyzed using either pseudo-dynamic (Newmark-based) or coupled elastoplastic continuum approaches. The most relevant damage mechanisms are those affecting watertightness. Zoned earth dams may develop seismic-induced fractures resulting from sliding through the core or from stress release associated with distributed deformation. Coupled analyses provide fundamental physical insight into the processes governing hydraulic fracturing under both seismic and post-seismic conditions, while pseudo-dynamic methods offer valuable information on potential sliding mechanisms and on whether failure surfaces are likely to propagate through the core. The integration of these two approaches enables a deeper understanding of core vulnerability and improves the overall reliability of seismic safety evaluations. This study explores these aspects through the analysis of the Conza Dam in Italy—a unique case where a major earthquake occurred during construction, and where comparative testing of original and recent materials revealed progressive changes in properties over decades of operation. The combined application of pseudodynamic and coupled dynamic analyses to this case demonstrates their complementarity and effectiveness in predicting potential earthquake-induced damage.

1. Introduction

In the design of a new dam, preliminary geological investigations are essential for determining whether the structure can be built, identifying the optimal location along the watercourse, and selecting the most suitable dam type (Gao et al., *2023*). For dams that have been in operation for decades, geological investigations must be updated and, in principle, extended to include the dam body itself (Azadi et al., *2022*). This is necessary because natural and man-made systems interact over time (often several decades), leading to physical and mechanical changes that must be assessed using integrated geological and geotechnical expertise. Both short and long-term deformation processes, particle migration, and various types of weathering induced transformations are typically observed in geological structures and must be addressed accordingly. To this end, the processing of monitoring data alongside laboratory and in-situ test results collected throughout the dam's lifespan is of primary importance (Pereira et al., *2018*). This step, among other objectives, helps ascertain whether events impacting the dam have caused deviations in its behavior compared to the assumptions made during the design phase—deviations that must be carefully considered when assessing dam safety and performing related numerical modeling. Additionally, comparing past and recent laboratory and in-situ tests provides valuable insights into potential changes in the dam's operational behavior.

In zoned earth dams, for instance, material property alteration over time can result from deformation-consolidation and erosion phenomena (Choudhury et al., *2025; Deng et al., 2025)*. The former are caused by the embankment dead load on the foundation soil interacting with the dam body itself, and eventual strong-motion earthquakes occurred in proximity to the dam site (Beiranvand and Komasi, 2021). The erosion phenomena may consist of suffusion leading to hydraulic conductivity variation (Chen and Zhang, 2023), particle removal along soil-concrete interfaces subjected to concentrated seepage and erosion in core fractures that experience leakage (Deng et al., *2025*). Hydraulically connected fractures throughout the core may arise from hydraulic fracturing or global instability phenomena (Sherard, *1986*).

* Corresponding author.
E-mail address: stefsica@unisannio.it (S. Sica).

https://doi.org/10.1016/j.enggeo.2026.108559
Received 4 August 2025; Received in revised form 18 November 2025; Accepted 12 January 2026
Available online 13 January 2026

In the seismic safety assessment of an old earth dam, these preliminary activities are indispensable (Chen et al., *2014*; Wang et al., *2021*).

A zoned embankment with coarse-grained shells is typically not susceptible to global instability under static loading conditions, but it may experience sliding during seismic shaking, especially when ground acceleration exceeds 10% to 20% of gravitational acceleration (ICOLD, 2002). Although global stability is usually restored after the earthquake, impounding can adversely affect the dam during the post-seismic phase if the seismic event generates sliding surfaces that intersect the core, potentially creating pathways for leakage and internal erosion. Core filters remain effective in tackling erosion as long as the sliding displacement does not excessively displace the filters, compromising their spatial continuity (Pagano et al., *2019*).

According to Sherard *(1986)*, hydraulic fracturing involves the wedge action of impounding pressure, which propagates a fracture throughout the core by overcoming the resistant action of the normal stress compressing the potential fracture path. Normal stress may drop due to stress transfer mechanisms from the core to the shells (arching). Arching, which arises from deformation when the shells are stiffer than the core, may be enhanced during any stage involving dam deformation, including earthquake and post-seismic consolidation (Sica and Pagano, 2009).

Complete (advanced) analyses of an earth dam, based on coupled elastoplastic continuum models, provide all the physical quantities required to assess and verify the dam seismic and post-seismic safety conditions. Simulating static and seismic stages can also aid in interpreting dam observations through back-analysis, offering an effective, data-driven calibration of model parameters, as emphasized by Sica et al. (2008). Complete analyses are particularly well suited for computing stress components that provide insights into hydraulic fracturing susceptibility and permanent deformational patterns, which feature the overall level of dam damage. However, when performed using conventional procedures, these analyses, are less effective in capturing deformation mechanisms associated with shear strain localization and the development of surface sliding.

On the other hand, the Newmark *(1965)* method and its derivatives are well-suited for analyzing sliding patterns (Papadimitriou et al., *2014*) and the stability of earth dams (Casablanca et al., *2022*). Specifically, the results they provide indicate whether sliding surfaces could form across the core, the magnitude of sliding displacements, and how these aspects could affect filter functionality *(*Pagano et al., *2019)*. This information can serve as supporting or complementary data to enhance the interpretation of stress states and damage levels provided by complete analyses. By combining their respective strengths, complete analyses and Newmark-based methods offer a more complete understanding of core vulnerabilities, thereby improving the overall reliability of the seismic safety assessment.

The paper reverses a long-standing paradigm in the analysis of zoned earth dams, which traditionally considers pseudo-dynamic approaches hierarchically below fully coupled dynamic analyses. It demonstrates, instead, that the two approaches, addressing different damage mechanisms, operate in synergy and provide complementary insights. The analysis of the Conza Dam, a zoned earth dam built in Southern Italy between the 1980s and 1990s, is adopted as a reference to illustrate this concept.

The case study in itself presents several original features. Its construction coincided with the 1980 Irpinia earthquake (Mw = 6.9), when the embankment had reached about one-third of its final height, providing the first documented evidence of a dam body damaged by an earthquake during construction and partly raised on a seismically deformed embankment, in a sequence intriguing in being interpreted empirically and numerically. Geological investigations documented a rare and interesting co-seismic settlement pattern, which extended across the entire dam site and required considerations about its role in the assessment of the dam's seismic behavior. Finally, the case study documents through comparison between old and recent tests on dam's materials how the seepage process modified material properties over decades of operation.

The paper analyses the seismic behavior of the Conza Dam under shaking scenarios based on indications provided by the current Italian technical standards - NTD14 (MIT, 2014) and NTC18 (MIT, 2018) - guidelines (DGD, 2019), and according to recent seismological studies. Preliminary, the case study is presented, based on monitoring data collected from the early construction stages up to recent years. These data include a comprehensive overview of the 1980 Irpinia earthquake's impact on the dam, well documented based on cross-arm measurements taken from various sections of the embankment. The illustration of the case study also considers a detailed discussion of the mechanical characterization of dam materials and the evolution of their properties over the past four decades. Coupled analyses are carried out to simulate in a unified manner, through a single predictive tool, the complex sequence of including the first phase of construction, the 1980 Irpinia earthquake, the second phase of dam construction, the consolidation under the action of impounding until steady state, and finally, the scenario earthquakes. Finally, the paper discusses the results of both advanced analyses and Newmark-based methods, with emphasis on their synergistic application for interpreting seismic-induced damage mechanisms in zoned earth dams.

2. The Conza Dam

2.1. Geological and geotectonic context

The Conza Dam (Fig. 1a) is located on the Ofanto River, near the border between the Campania and Puglia regions, specifically in the Avellino Province, approximately 120 km east of Naples. It is one of the largest reservoirs in the southern Apennine range.

At the dam site, the marked predominance of clayey soils (Fig. 1b) has promoted the genesis of a broad valley basin, characterized by an overall gentle morphology with smooth and flared slopes.

The middle and lower valley flanks are generally gentle slopes, with a slight increase in degrees on the right-hand side of the river (southern slopes), due to the layers standing in a dip-slope configuration.

The outcropping soils in the dam area consist of a heterogeneous formation mainly composed of the so-called “Varicolored Clay”. Over this formation, in stratigraphic discontinuity, lie clastic deposits belonging to two distinct sedimentary cycles: one of Pliocene age, consisting of basal conglomerates and blue clays, and a second of Pleistocene age, composed of conglomerates, clays, and sands. Finally, alluvial deposits of the Ofanto River are recurrent, consisting of recent alluvium and terraced alluvium in multiple orders.

More specifically, the northern slope of the valley is characterized by the presence of a Pliocene clay formation, consisting of thinly bedded, homogeneous, blue-gray, fossiliferous clays, occasionally interbedded with sandy and polygenic conglomerate lenses (Fig. 2). Recent alluvial deposits are found along the Ofanto valley floor, whereas colluvial deposits outcrop on the southern slopes, overlying a clayey–calcareous–arenaceous flysch.

The main tectonic regime of the area is predominantly extensional, characterized by normal faults with prevailing E–W-oriented fault planes that bound the region. The Ofanto Valley itself aligns with these principal tectonic trends.

The significant tectonic dislocation along these faults during the

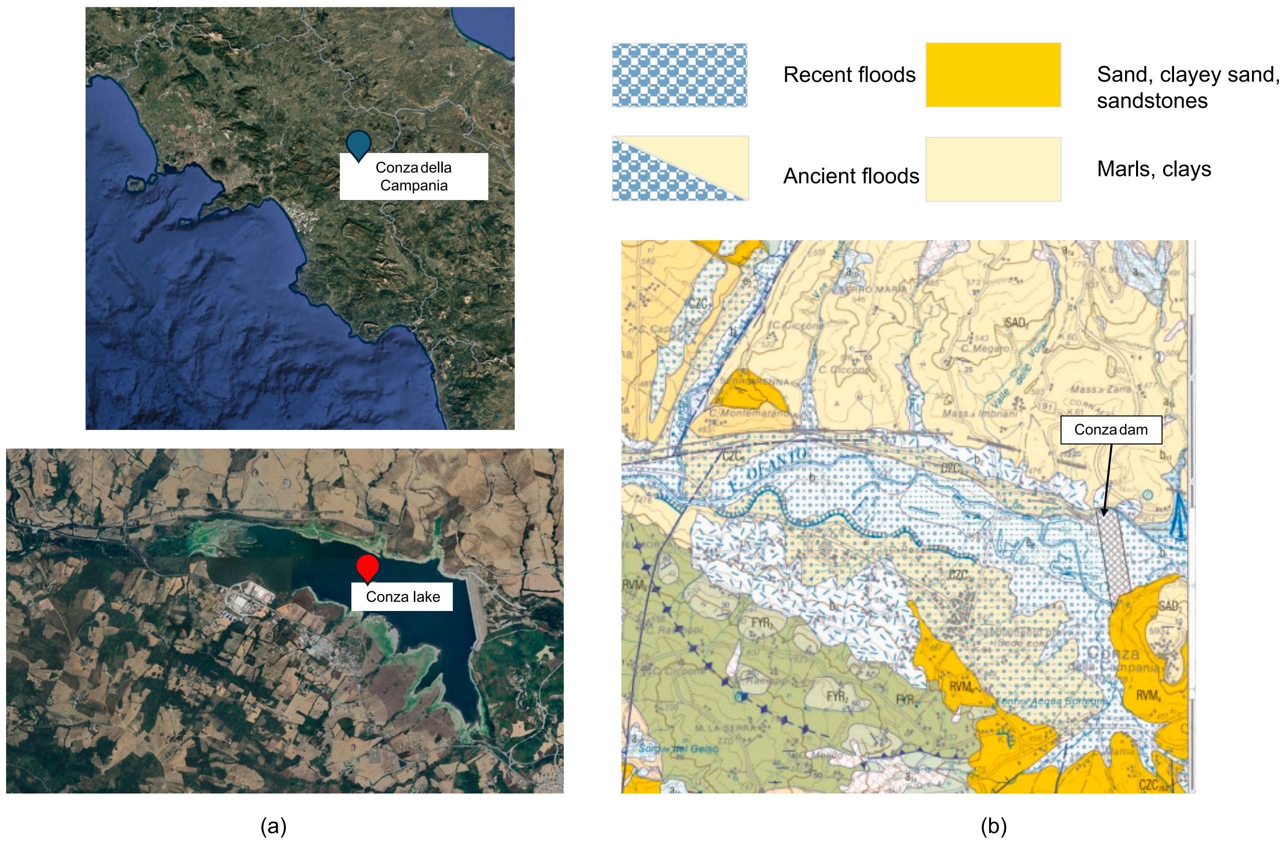

Fig. 1. – Location and view of the Conza lake from Google Earth (a), geological details at the dam site (b).

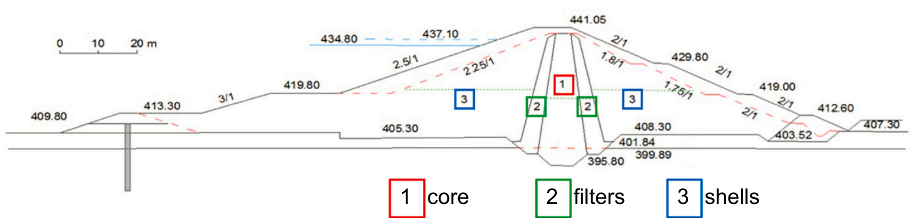

Fig. 2. Cross section of the Conza Dam.

Pleistocene age induced widespread settlements and consequent topographic lowering of the area considered. The Ofanto valley thus corresponds to a tectonic depression that progressively acquired the morphological features of a valley under the effects of sequential tectonic dislocations.

2.2. General information about the dam

The Conza dam is a zoned earth dam with an internal clay core (see Fig. 2). The dam was constructed between 1979 and 1988 to create a reservoir with a capacity of 77.40 million cubic meters. Consistently with the geological description of the previous paragraph, the foundation subsoil consists of an over-consolidated clay deposit extending down to hundreds of meters, in some areas covered by alluvia. The maximum height of the dam is about 47 m, measured from the deepest core foundation level, which is situated directly atop the clay deposit. The core is a medium plasticity clay, while the shells are coarse-grained materials sourced from alluvial deposits. Shells are found either on top of the clay deposit or, sometimes, on the alluvial deposits where they are present. The material for the core filters is derived by removing the coarser gravel component from the alluvial material. The dam develops longitudinally along 880 m with a cross-section largely repeated along the embankment length, except for variations in thickness of the alluvial layer.

2.3. Dam history under static and seismic conditions

Fig. 3 illustrates the evolution of fill and impounding levels over time. Vertical dashed lines denote key episodes in the dam's history. Construction started on 7 August 1979, filling the trapezoidal excavation for the core foundation and placing the first layers of shells after removing the soil-vegetated cover, which was approximately 1 m thick.

Construction was suspended due to the 1980 Irpinia earthquake, whose epicentre was located close to the dam site. At that time, the shells had been raised to about 15 m (with the top reaching 420 m above sea level), while the core was 5 m lower than the shells. Two sections of the dam had not yet been built. One near the left abutment, was awaiting the rerouting of a railway crossing the dam footprint. The other, 120 m long, was located in the central part of the dam, where the watercourse had not yet been diverted.

The 1980 seismic event was 6.9 in Richter magnitude, with a total duration of about 80 s. Seismological studies conducted by Bernard and

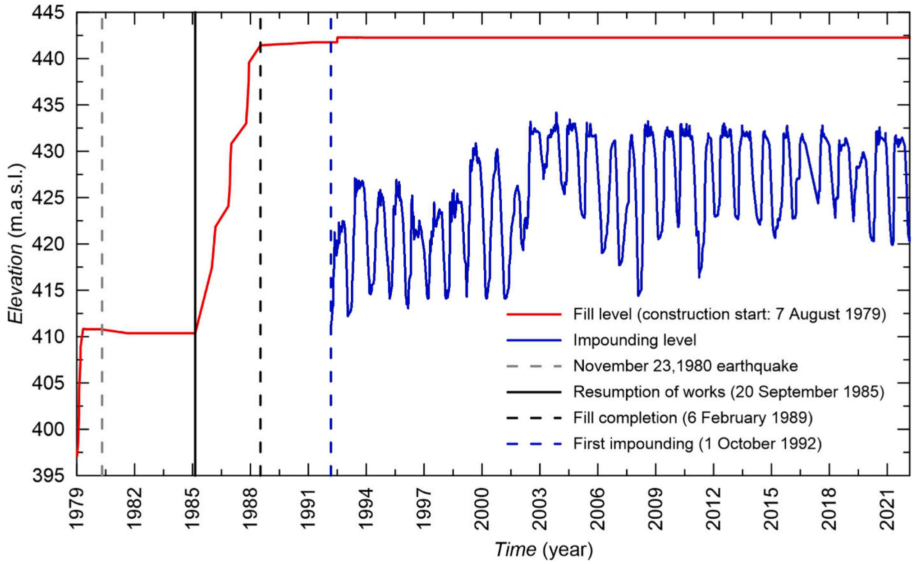

Fig. 3. Evolution of fill-impounding levels and main episodes affecting the dam life.

Zollo *(1989)* interpreted the global event as composed of three distinct sub-events partly overlapping. Consistent with the tectonic framework described in the previous paragraph, a sequence of NW–SE oriented faults was activated, resulting in strong ground shaking (as recorded at the nearby Calitri station) and causing widespread ground subsidence throughout the Ofanto Valley (Dello Russo et al., *2017*). In Fig. 4, three time instances ($t = 0$ s, 20 s, and 40 s) represent the sequential activation of three distinct fault segments, parallel to one another and extending over approximately 40 km. The first sub-event propagated bi-directionally, while the other two were uni-directional. The dam was located 5 km from the epicentre and just a few hundred meters from the fault responsible for the third sub-event. It experienced visible deformation, which was quantified through topographic and cross-arm measurements taken shortly after the event (see § 2.5).

During the construction pause, the dam cross-section was redesigned according to the updated Italian Seismic Regulations (D.M., 1982), which increased the seismic hazard at the dam site. The new cross-section (see Fig. 2) was conceived 2 m higher, with reduced slope angles and a widened crest. Fill placement restarted in December 1983 and ended in July 1988. The first impounding began on October 1, 1992, marking the dam transition into operation. Since then, the dam has experienced repeated yearly fluctuations in the impounding level.

At the downstream toe of the embankment, a drainage trench intercepts reservoir water seeping through the dam to quantify seepage flows. In December 2000, a concrete sheet pile wall extending to the clay deposit was constructed downstream of the trench to prevent water from the downstream phreatic groundwater from infiltrating the trench.

2.4. Embankment and foundation materials

In 2019, three pairs of new boreholes were drilled in the middle section of the dam. One extends from the crest axis down to 40 m in the core. Another goes from the crest upstream edge through the upstream shell and part of the filter, reaching a total length of 30 m (Fig. 5a). The third develops from the first downstream bank, traverses the downstream shell, and enters the shallow foundation soils for a total of 30 m (Fig. 5b). After stratigraphic identification and the extraction of undisturbed samples, each borehole pair was then employed to conduct cross-hole tests.

The clay core consists of sandy silt with clay. Grain size tests, both recent and older (Fig. 6), showed consistent results across all fractions. However, the clay fraction was not detailed experimentally. In contrast, discrepancies were observed in the plasticity properties (Fig. 7). While older tests reported an average plasticity index of 20% and a liquid limit of 40%, recent tests showed a significant decrease to 5% and 30%, respectively.

The interpretation of Consolidated Isotropically Drained (CID) and Undrained (CIU) triaxial tests conducted on undisturbed samples yielded the following mean values:

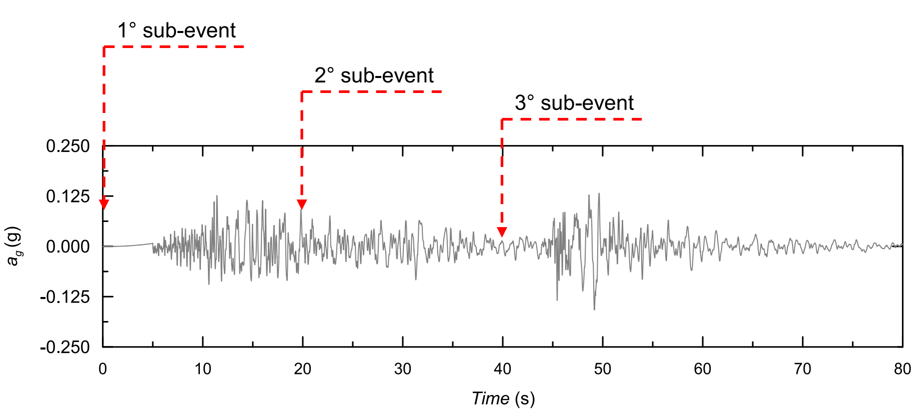

Fig. 4. Acceleration time histories recorded at the Calitri station during the Irpinia event of November 23, 1980.

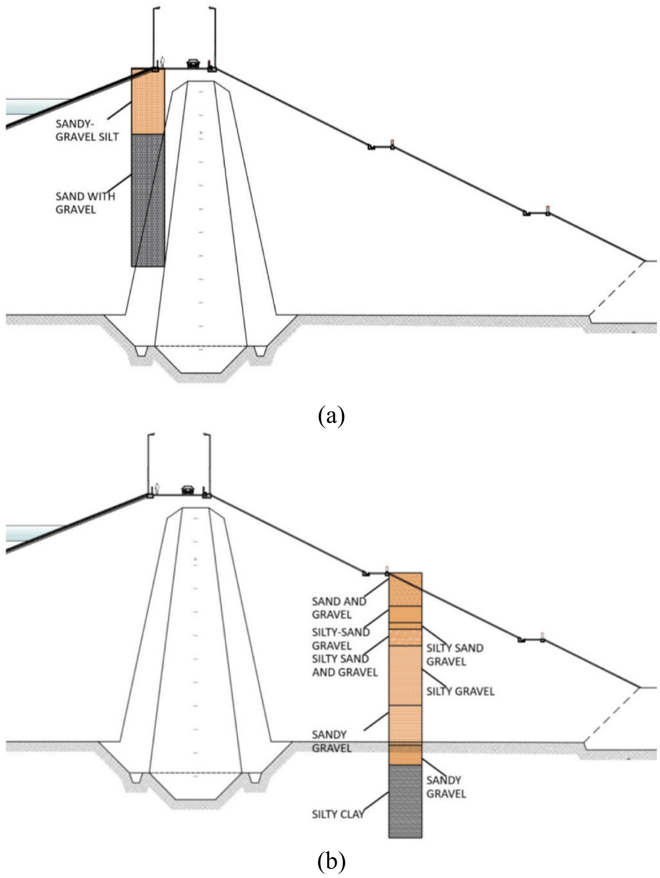

Fig. 5. Stratigraphy obtained from the new boreholes drilled in the upstream (a) and downstream (b) shell.

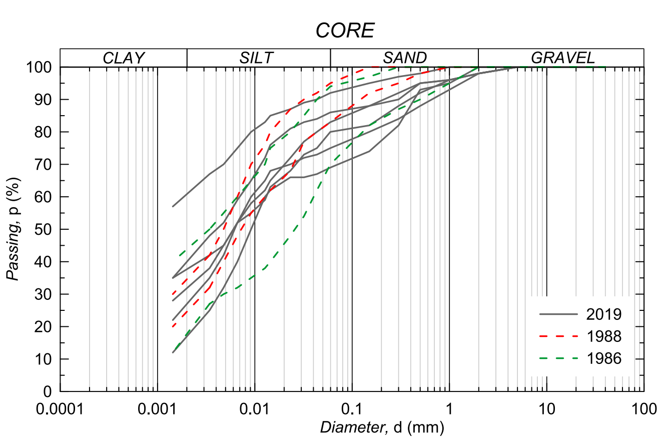

Fig. 6. Grain size distributions of the core material from old and recent tests.

- φ' (friction angle) = 22.6°
- c' (effective cohesion) = 45.5 kPa
- c_u (undrained cohesion) = 146.9 kPa

The hydraulic conductivity coefficient, estimated averaging results from oedometric tests, resulted equal to $2.9 \cdot 10^{-11}$ m/s.

The old filter material, classified as sand with gravel (Fig. 8), resulted in a much finer and more heterogeneous composition in recent tests, ranging from silt with sand and clay to gravelly-silty sand. Consistently, the old non-plastic soil turned into a medium plastic material, showing a plasticity index equal to 22.5%.

CID triaxial tests conducted on undisturbed samples yielded the

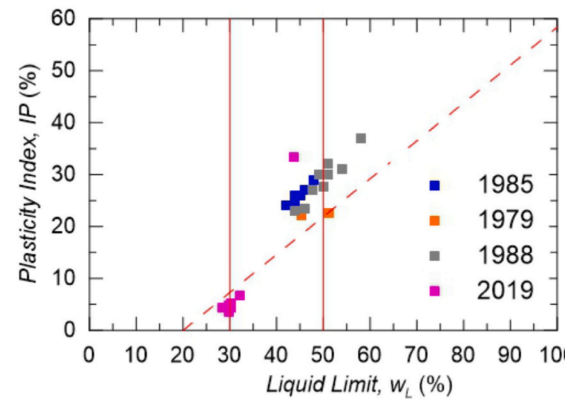

Fig. 7. Index properties of the core material from old and recent tests, represented on the Casagrande plasticity chart.

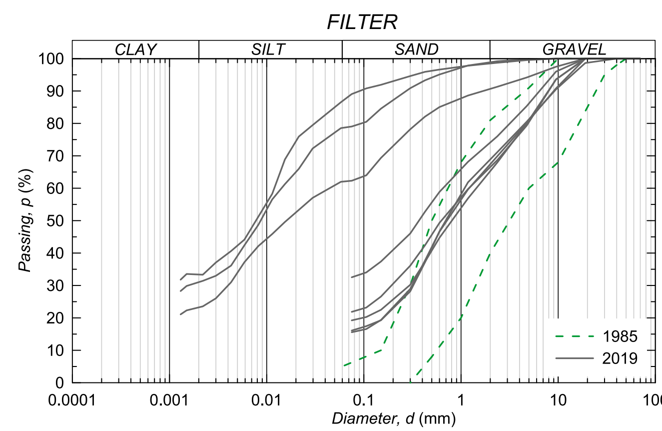

Fig. 8. Grain size distributions of the filter material from old and recent tests.

following mean strength parameters:

- φ' = 23.1°
- c' = 43.5 kPa

The hydraulic conductivity coefficient, estimated from variable head permeability tests, averaged $6.4 \cdot 10^{-6}$ m/s.

In older tests, the shell material was characterized as silty sand with gravel. However, recent tests revealed significant modification, showing notably higher percentages of silt and sand fractions (Fig. 9). Direct shear tests conducted on large samples yielded the following mean strength parameters:

- φ' = 44°
- c' = 8.8 kPa

The hydraulic conductivity coefficient, estimated from variable head permeability tests, averaged $4.7 \cdot 10^{-6}$ m/s.

The foundation subsoil is an overconsolidated silty clay with medium plasticity. Grain size distribution and plasticity properties remained unchanged over the years. Strength parameters obtained from averaging all CID triaxial test results are:

- φ' = 19.7°
- c' = 55.6 kPa

The hydraulic conductivity coefficient, estimated from oedometric tests, averaged $2.2 \cdot 10^{-11}$ m/s.

The cross-hole tests indicate that the core shear wave velocities

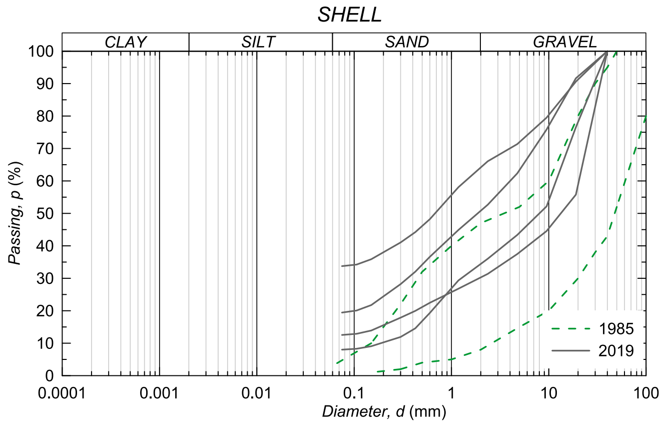

Fig. 9. Grain size distributions of the shell material measured in old and recent tests.

(Fig. 10) range between 300 and 400 m/s in the first 10 m, decrease around 200 m/s between 10 and 25 m, and finally increase again slightly below 25 m. The higher velocity in the uppermost part can be attributed to the presence of a different material covering the core, made stiffer than the core by coarser fractions, and suction levels for elevations above the zero-pore-water-pressure line (Pagano et al., *2024*). The reduction in velocity observed from the depth of 10 m down is induced by pore water pressure increases and likely stress transfer mechanisms from core to shells (core arching), both decreasing the mean effective stress levels and, consistently, core shear stiffness (Pagano et al., *2008*).

In the upstream shell, the trend of shear wave velocity also decreases with depth due to the progressive changes in pore water pressures, at the highest positions above the water table occurring in the negative range (suction) and at deeper positions, below the water table, in the positive range.

Finally, velocities in the downstream shell are generally higher than those in the upstream shell, likely due to higher suction levels.

2.5. Monitoring data

The dam is equipped with instrumentation to acquire most of the physical quantities typically observed in zoned earth dams, such as internal settlements (USBR cross-arms), topographic surface displacements, pore water pressures within the core (vibrating wire piezometric cells) and the subsoil (tube piezometers), total vertical stress (vibrating wire load cells), and seepage flows (downstream through a draining trench at the embankment toe). The monitoring setup (Fig. 11) is primarily focused on six cross-sections of the dam.

The paper presents only a limited subset of the available measurements, selected as representative of the overall dam behavior. The general aim is to determine, for the purpose of characterizing the seismic response, whether the dam exhibited normal and steady behavior under static conditions—free from anomalies—or whether structural weaknesses are present that should be considered in predicting its performance. Part of these data has also been used as a reference for recalibrating the model parameters (see Section 5.1).

2.5.1. Settlements

For a comprehensive analysis of dam settlements over the extended lifespan of the Conza Dam, the following three figures are essential.

Fig. 12 plots the settlement profiles recorded at the cross-arms installed in Sections 2 and 3 (Fig. 11a) over a 40-year period.

Fig. 13 presents the settlement evolution at three markers of the same cross-arms, located at the Core Foundation (CF), Core Crest (CC), and Core Top at the time of the 1980 Earthquake (CTE). This Figure also displays the settlement evolution of the Downstream Shell Foundation (DSF), observed through cross-arm plates positioned at the shell-ground interface.

Finally, Fig. 14 displays the CF and CTE settlement profiles measured

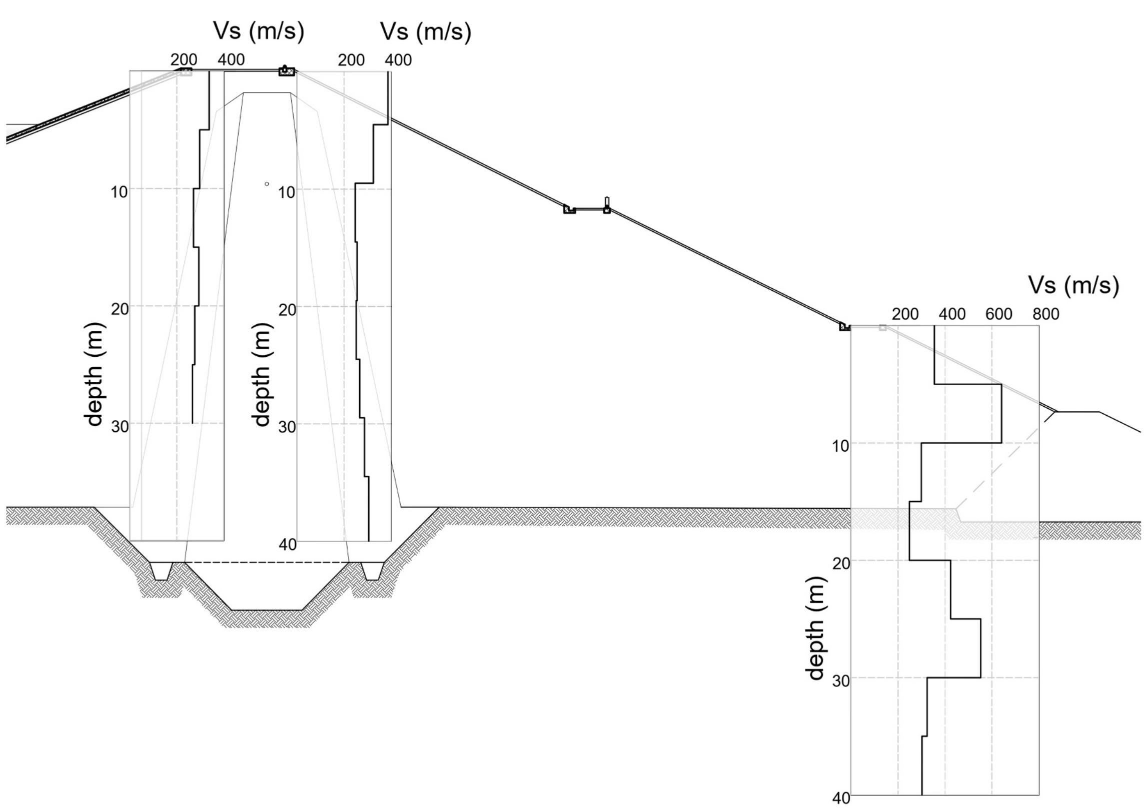

Fig. 10. Shear wave velocities in the core (central plot), upstream (left) and downstream (right) shell.

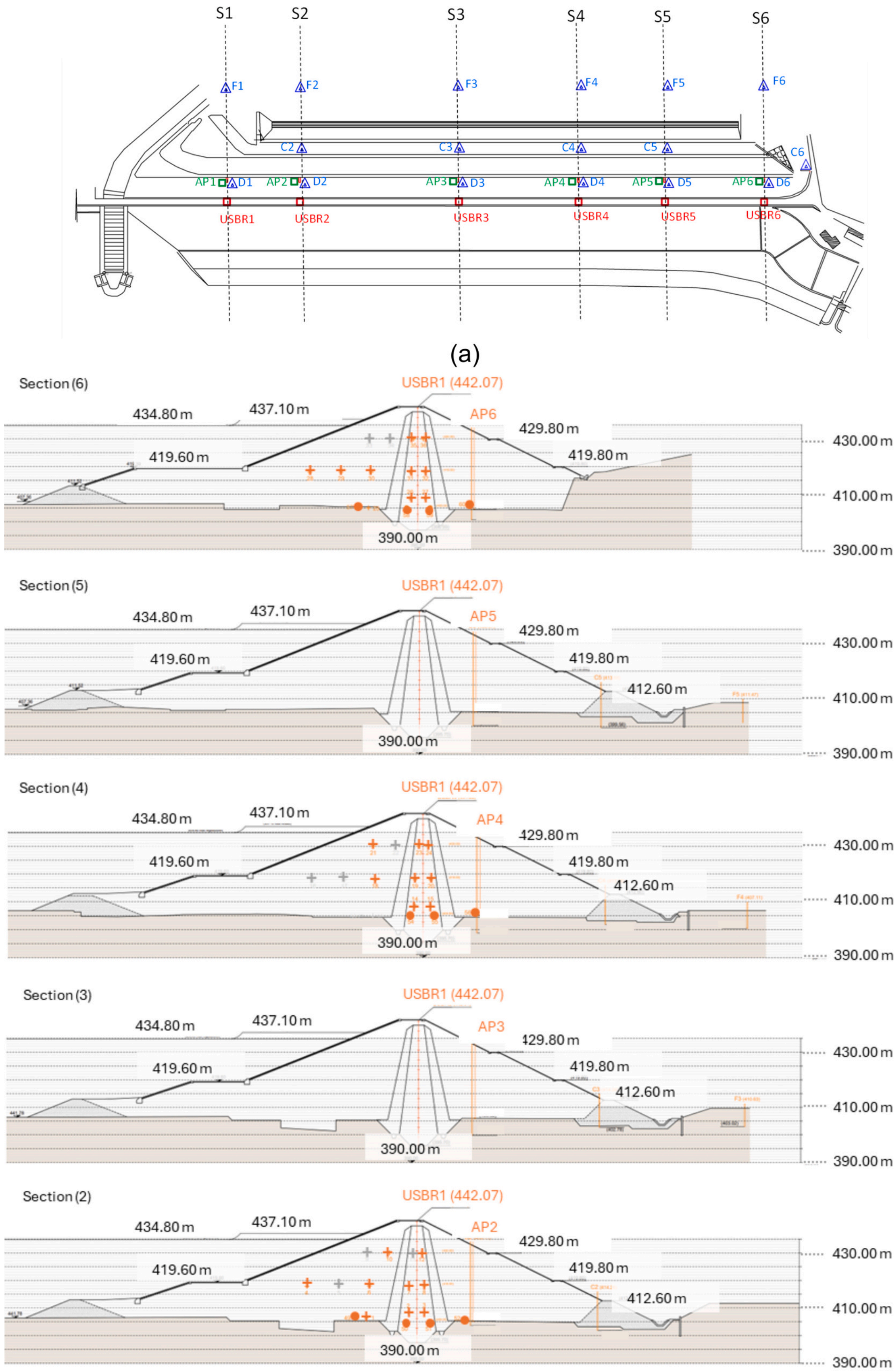

Fig. 11. Monitoring devices installed in the Conza Dam: (a) plan view of the instrumented cross-sections with position of cross-arms (USBRi), plate cross-arms (APi), subsoil tube piezometers (Ci and Fi); (b) instrumented cross sections indicating position of piezometric cells, load cells and cross-arms.

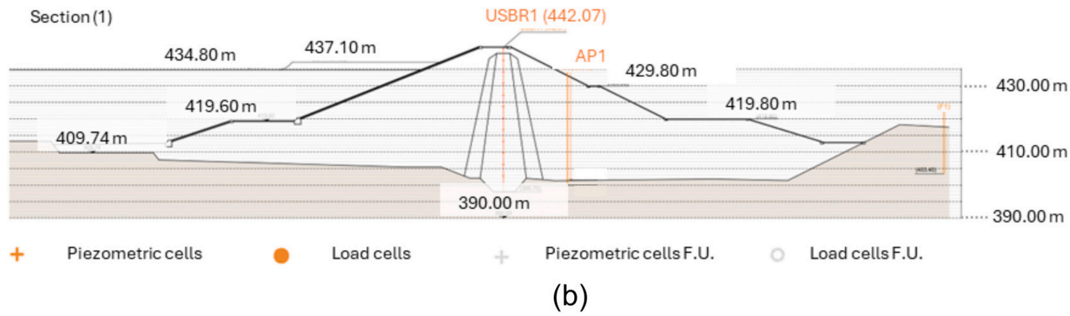

Fig. 11. (*continued*).

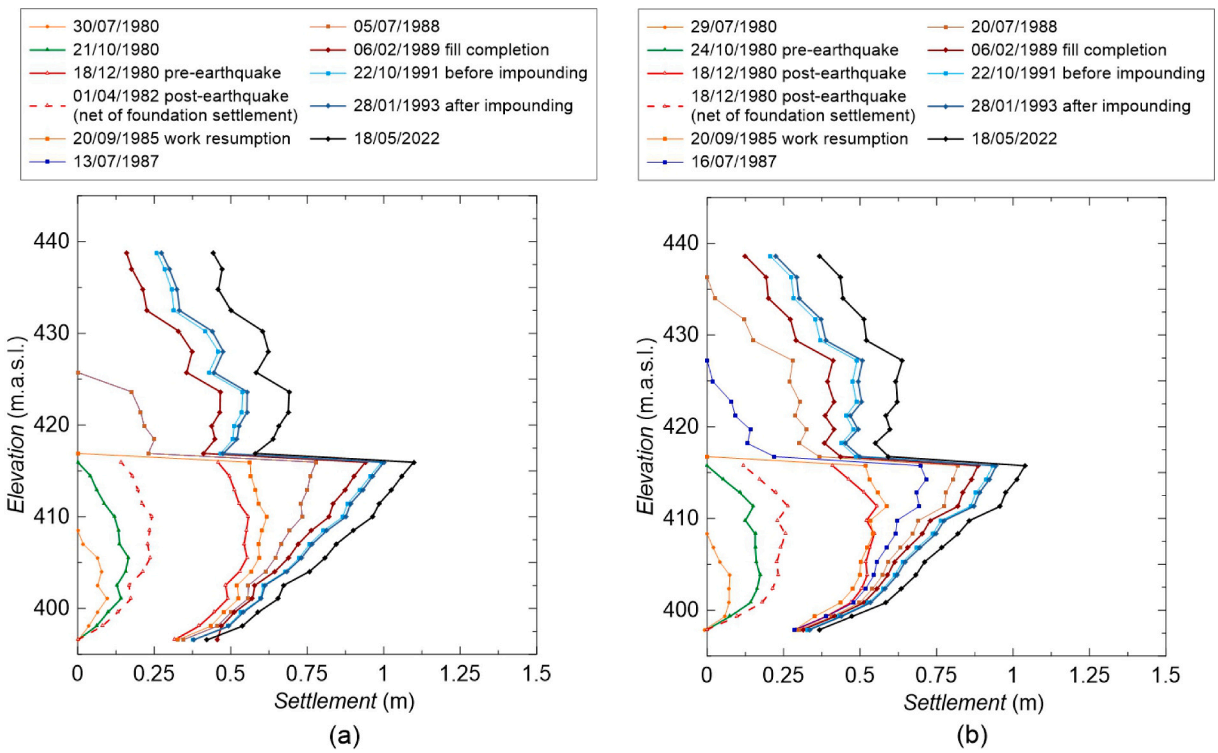

Fig. 12. Settlement profiles measured at the core axis of (a) Section 2 and (b) Section 3.

longitudinally by cross-arm markers across five of the six-instrumented sections. Settlements are calculated relative to a zero reference measurement, which corresponds to the first records taken just before the 1980 earthquake. The distance between the CF and CTE patterns quantifies the seismic-induced embankment shortening.

From the beginning of embankment construction until the last record date before the earthquake, settlement profiles (Fig. 12) result in parabolic shapes symmetrical to the fill mid-height, consistent with Marsal's theoretical curve (Marsal et al., *1950*). The settlements at the Core Foundation (CF) are minimal. Occasionally, slight CF uplifts are observed (refer to Fig. 13 as well) as consequences of the non-uniform application of embankment dead load, determined by shells raised systematically ahead of the core, and undrained reaction of the subsoil preserving volume invariance.

The subsequent period begins with the seismic event in 1980, followed by the 1980–1985 standby in construction and the 1985–1988 work resumption until the dam completion.

A synoptic analysis of Figs. 12 to 14 reveals that the seismic-induced deformation is significant. Settlement profiles result shifted due to CF settlement and, at the same time, tilted because of fill shortening (these two components are also displayed separately in Fig. 12). The CF settlements are not uniform longitudinally (Fig. 14a), increasing towards the right abutment, while the embankment shortenings displayed as spread between the two curves result in almost constant, with a slight reduction observed in the middle due to the lower embankment level (and transmitted load) accommodating the fill lack at and near the river path. Maximum CF settlement is 40 cm, while maximum embankment shortening is 18 cm. The former value is consistent with ground settlements observed diffusely across the entire valley. Various technical and research works (e.g., Cotecchia et al., *1990*; Dello Russo et al., *2017*; Sica and Dello Russo, 2021) attribute these ground settlements to co-seismic dislocations activated by the extensional tectonics illustrated in § 2.1 and, marginally, to compression of the clay deposit.

Settlements exhibit abrupt discontinuities in their evolution due to the earthquake (Fig. 13). The spread between DSF and CF at the earthquake time approximately estimates the seismic-induced shortening of the alluvial deposit where present. It results negligible in all sections.

Deformation is negligible everywhere over the post-earthquake standby. Upon work resumption, settlement profiles bend downward as they reflect strains in the lower embankment zones larger than in the higher, being the lower additionally deformed by the earthquake. With increasing dead load, CF and DSF settle slightly, according to the trend

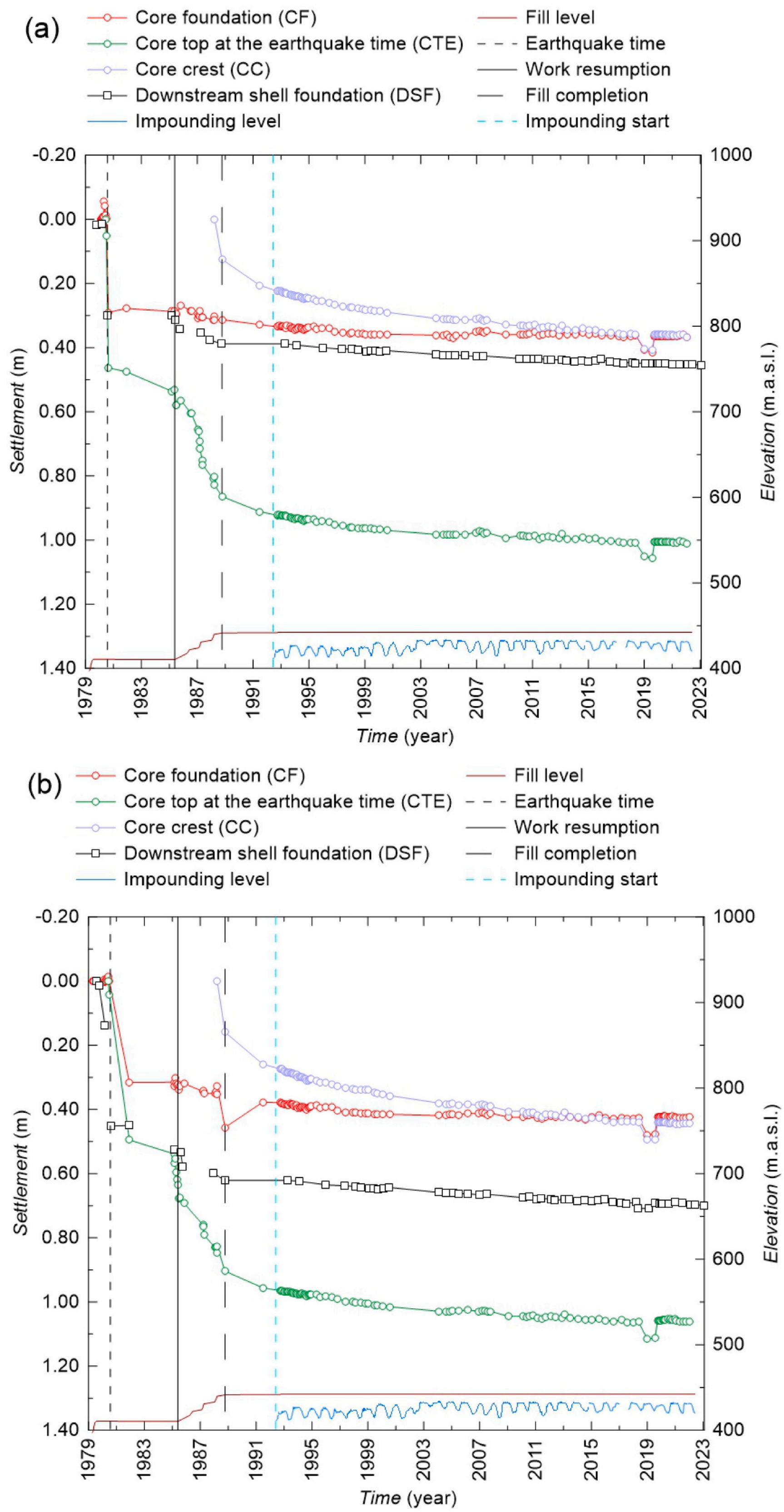

Fig. 13. Evolution of settlements measured at three selected cross-arm markers along the core axis and at the cross-arm plate installed in the downstream shell foundation; (a) Section 2, (b) Section 3.

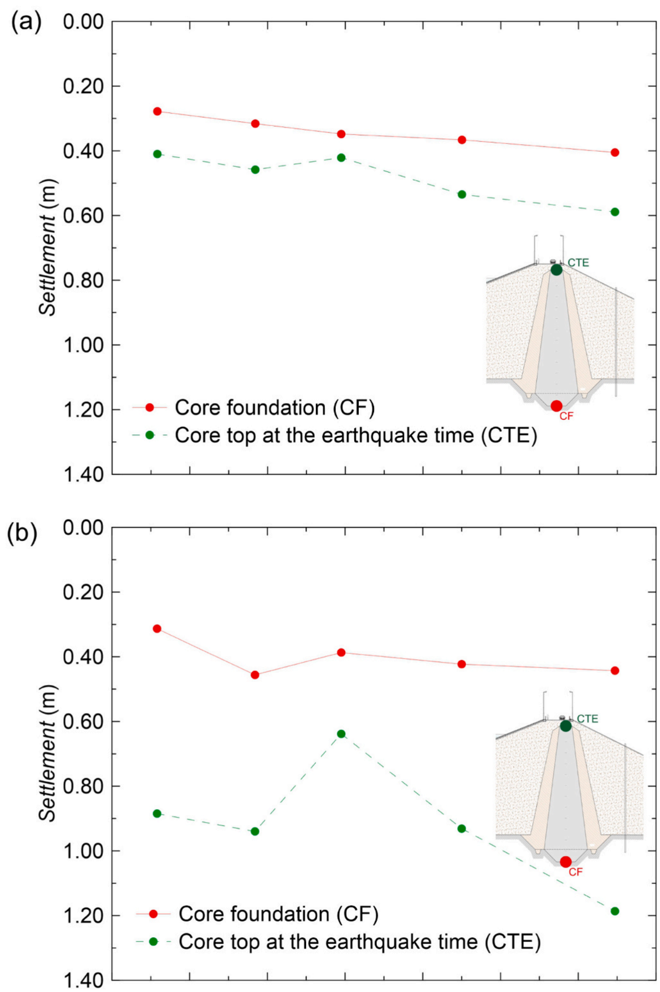

Fig. 14. Longitudinal settlements measured along the Core Foundation (CF) and the Core Top at the Earthquake time (CTE) at two different stages: (a) just after the earthquake and (b) at the end of construction (settlements are relative to a reference time just before the earthquake event).

in place before the earthquake, while the fill experiences shortening.

Over the post-construction consolidation stage following dam completion and preceding first impounding, CF and DSF settlements remain negligible, while the fill shortens by about 10 cm (equivalent to 0.2% of average vertical strain), emerging as further tilting of all profiles. Deformation is primarily a consequence of core hydraulic re-equilibrium, stemming from excess pore water pressures raised during construction.

Throughout the long dam operation (from the first impounding until May 2022), the settlement trend progresses according to the previous pattern, with negligible CF and DSF increments and slight embankment shortenings, likely driven by secondary consolidation phenomena.

2.5.2. Total stresses

In zoned earth dams, total stresses are monitored to quantify core stress discharge. This originates from the stiffness contrast between the core and shells, which poses a risk of hydraulic fracturing. Typically, this monitoring involves tracking vertical stresses along horizontal lines crossing the core and shells, as was done for the dam in question. Fig. 15 illustrates the distribution of total stress displayed by four pressure devices crossing the core and shells in the lower zone of Section 2. The

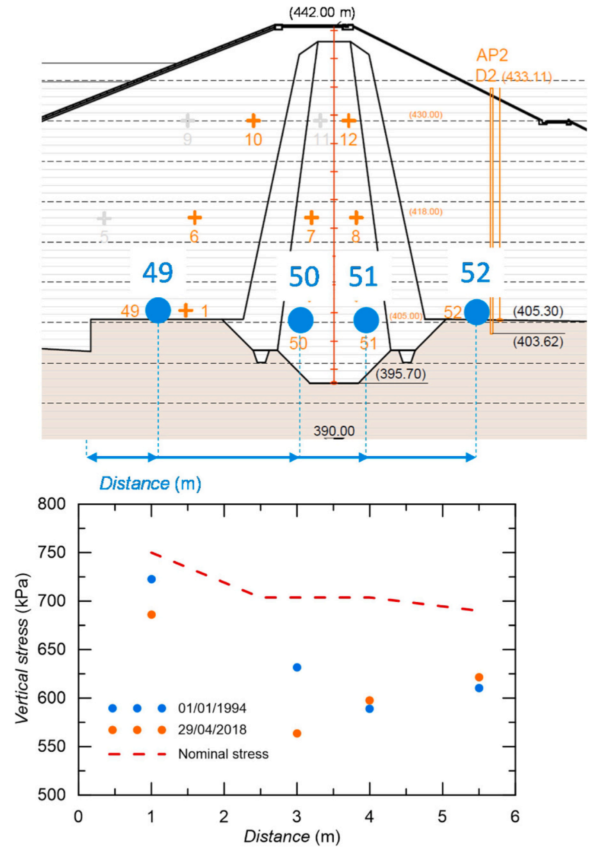

Fig. 15. Total stresses measured in Section 2 at two different times.

measurements refer to the period 1994–2022, following the completion of the dam impounding. Additionally, at the same cell elevation, the figure displays the distribution of nominal total stresses computed from the weight of the overburden material. Notably, all monitored values remain below the nominal levels, indicating a lack of vertical equilibrium in considering a stress distribution linearly linking the experimental points. This is not surprising as total stress monitoring in soil systems faces challenges regarding representativeness and device disturbance (Pagano et al., 2006), affecting the reliability of the measured values.

Measurements in the core deviate more from nominal values than the shells, suggesting some core discharge. The measurements are generally stable over time, except at the upstream measurement point in the core, where stress tends to decrease over time.

2.5.3. Pore water pressures and seepage flows

A few pore water pressure measurements were taken around the time of the 1980 seismic event, using the piezometers installed in the alluvium deposits. These measurements indicate that the Irpinia earthquake induced a few kPa increments in pore water pressure, an expression of a contractive reaction upon shearing of the foundation clay deposit. Continuous monitoring of pore water pressures was conducted later, between the beginning of the impounding stages in 1992 and 2018, when records were interrupted. Measurements were carried out in both the embankment and subsoil at Sections 2, 4, and 6 and in the subsoil only at Sections 3 and 5.

The observations display evolution and distribution consistent with dam reaction to impounding fluctuations. In the upstream shell, piezometric heads match impounding levels, indicating that the material has

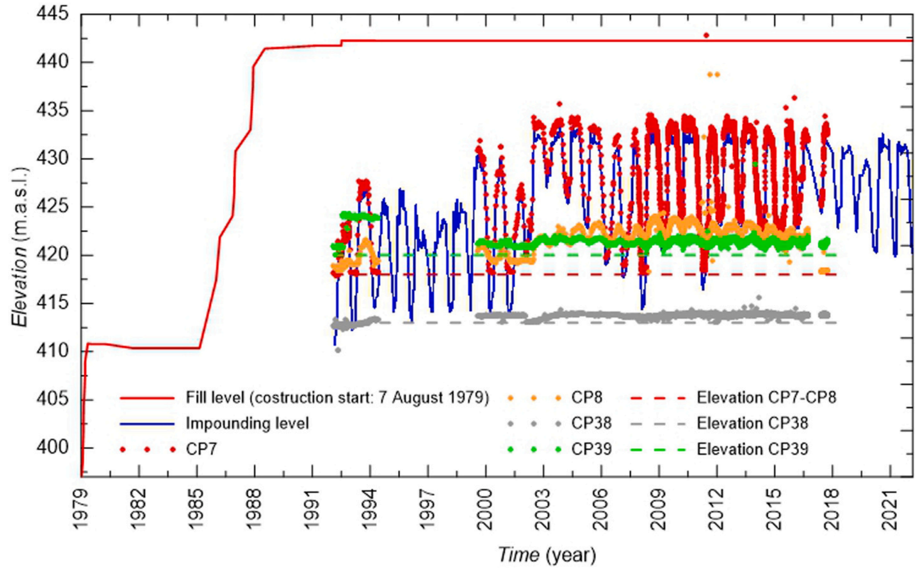

Fig. 16. Pore water pressures measured in the core by four piezometric cells (CP) positioned at mid-height of Section 2.

preserved over the years high hydraulic conductivity assuring a free-draining behavior.

In the core, measurement points located near the upstream edge also indicate, as in the shell, piezometric head matching the impounding levels (Fig. 16). In contrast, those positioned centrally and downstream show significantly lower values, consistently with a downstream-oriented seepage process. Pore water pressures measured in the downstream foundation soils exhibit only slight positive fluctuations, with trends appearing not related to impounding fluctuations. Seepage flow measurements are regular and negligible, not exceeding 1.5 l/s.

3. Modeling the boundary value problem

3.1. Criteria for the selection of Interpretative–Predictive numerical models

Overall, the dam mechanical response derived from the empirical interpretation of monitoring data is consistent with that expected from simple behavioral models and appears free from specific anomalies. This implies that the assessment of seismic performance can be reliably conducted using predictive tools that capture the overall response of the dam body, assuming the absence of significant structural flaws and adopting modeling ingredients consistent with the phenomena evidenced by the measurements.

In line with advanced international standards and guidelines, Italian dam regulations NTD14 (MIT, 2014) and NTC18 (MIT, 2018) require that seismic assessments be performed to evaluate the structural response of dams to site-specific earthquake scenarios. The verification must address key response mechanisms, including seismic-induced deformations (e.g., freeboard loss and slope instability), generation of excess pore water pressure (liquefaction), and stress release within the core (hydraulic fracturing). Such assessments require quantifying strain and stress distributions, as well as the evolution of pore water pressure throughout the dam body and the underlying foundation soils that interact with the embankment. Estimating these quantities inherently involves solving a continuum boundary value problem.

For the Conza Dam, long-term monitoring data — including observations from the 1980 Irpinia earthquake — clearly indicate that the dam experienced permanent deformations under static loads and their combined action with seismic shaking. These deformation patterns were not indicative of global sliding, but rather associated with widespread plastic strains within the embankment body. Monitoring data also revealed that deformation processes in zones composed of fine-grained materials were delayed due to transient hydraulic re-equilibration phenomena. Furthermore, a significant portion of the dam embankment experienced loading under unsaturated conditions, where both stiffness and strength were affected by suction levels, as revealed by field tests. These observations collectively underscore the need to adopt a coupled three-phase dynamic model implementing elastoplastic constitutive relationships as an interpretative and predictive tool. Geological and geotectonic investigations at the dam site also played a pivotal role in guiding numerical modeling choices. First, they helped define the extent of the soil domain—specifically the varicolored clay deposit—beneath the dam body, which could influence the alteration of the seismic signal as it travels upward from the bedrock to the embankment base. Second, these investigations indicated that the observed seismic-induced settlements at ground level were related to tectonic kinematics and only marginally caused by deformation of the clay layer and therefore should be excluded from numerical reproduction during the back-analysis phase of parameter calibration. Moreover, co-seismic tectonic kinematics, as they produce comparable settlements in both the dam body and the reservoir bottom while leaving the dam freeboard unchanged, are not expected to have any significant impact on the overall safety of the dam.

As discussed in the Introduction, the advanced numerical model has been complemented by a pseudo-dynamic, Newmark-type, analysis, intended to provide an estimate of displacements along potential sliding surfaces. This auxiliary method circumvents numerical ambiguities that may arise in fully elastoplastic simulations—particularly under strain localization—and provides displacement estimates grounded in empirical and theoretical frameworks well-established in engineering practice.

The subsequent sections first present the pseudo-dynamic analysis tool, followed by the advanced numerical model.

3.2. Pseudo-dynamic model

The pseudo-dynamic approach employed in this study utilizes a Newmark-derived method, as the accelerogram signal adopted to compute the sliding-block displacement (where the block represents the unstable mass W(S) sliding along a surface S) is the average (or equivalent) acceleration, $a_{eq}(t)$, acting on the unstable mass. This average acceleration was computed from an equivalent linear-viscoelastic analysis of the entire dam-foundation domain (Fig. 17), with the base

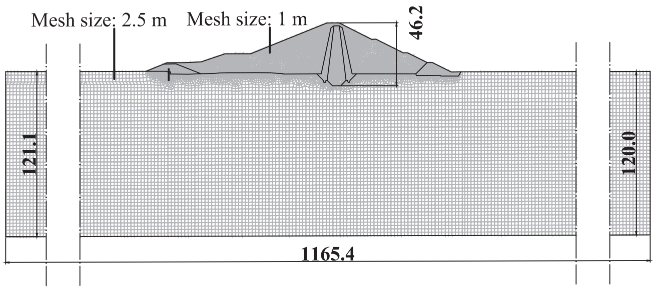

Fig. 17. Discretized geometry of the model used in the equivalent linear analysis.

subjected to the deconvolved input signals.

Processing the equivalent acceleration along the sliding surface, rather than the signal acting at the embankment base, accounts for the effects of dam deformability and damping on seismic wave propagation within the dam. This includes phenomena such as upward signal amplification or attenuation, as well as out-of-phase motion among different locations within the dam (Bilotta et al., *2010*).

Dynamic analyses were done using the finite element code Quake/W (GeoStudio, *2003*), which yields at each time the complete stress distribution, $\sigma'_{ij\text{-tot}}(t)$, as the sum of the static part, $\sigma'_{ij\text{-st}}$, and the dynamic, $\sigma'_{ij\text{-dyn}}(t)$, alteration induced by the earthquake.The $\sigma'_{ij\text{-dyn}}(t)$ component, only having the potential of causing permanent displacement, can be extracted from the complete stress distribution as net of the static stress quantified in advance by analyzing the dam subjected only to static loading conditions ($\sigma'_{ij\text{-dyn}}(t) = [\sigma'_{ij\text{-tot}}(t)-\sigma'_{ij\text{-st}}]$. The shear component of $\sigma'_{ij\text{-dyn}}(t)$ along S, $\sigma_{s\text{-dyn}}(t)$, if integrated along S, yields the force, $T_{dyn}(t)$, driving sliding along S. Dividing $T_{dyn}(t)$ by W(S) and multiplying this ratio by the gravity acceleration, results into the equivalent acceleration, $a_{eq}(t)$. At each time step, $a_{eq}(t)$ is related to a global instability safety factor, FoS(t), which is quantified assuming a normal stress distribution along S at the beginning of the shaking stage. Since the normal stress during the shaking is not updated, the dynamic increment results entirely applied to the water phase. When FoS equals 1, the critical acceleration, $a_{eq\text{-cr}}$, required to compute the permanent displacement using the Newmark procedure, is obtained. The sliding displacement direction aligns with the mean inclination of the S surface.

For each dam zone, values of G_0 were quantified at the mean value of the cross-hole velocity distribution measured across the zone (see Fig. 10). The decay of G/G_0 with increasing shear strain was defined based on the results of cyclic-triaxial and cyclic-simple-shear tests conducted for core and shell materials, respectively. Parameters of the clay material constituting the subsoil were quantified based on literature references (Vucetic and Dobry, 1991). The soil parameters adopted are summarized in Table 1.

The stresses under static, $\sigma'_{ij\text{-st}}$, and seismic, $\sigma'_{ij\text{-tot}}(t)$, conditions were estimated by analyzing the domain of Fig. 17. Before the dynamic analysis, the static effective stress was computed by applying the dead load and, separately, estimating the distribution of pore water pressures. Pore water pressures were computed assuming full impounding at steady-state (Fig. 18), consistently with trends in pore water pressure observations, highlighting that operational stages go through a sequence of fluctuating steady-state conditions. It is worth noticing that the increase in the finest fraction experienced by the downstream shell over decades, caused a reduction in its hydraulic conductivity and determined the zero-pore-water-pressure line throughout the shell rising a few meters above the dam foundation level.

3.3. Complete model

The complete dynamic model is based on the set of governing equations modeling the three-phase coupled dynamic approach (Costigliola et al., 2022). The finite element solution is performed by the code PLAXIS 2D (Brinkgreve et al., *2016*). Equations consist of:

– local dynamic equilibrium:

$$\underline{\underline{L}}^T(\underline{\sigma}' + \underline{m}S_e p_w) + \rho \underline{g} = \rho \underline{\ddot{u}}$$

where

$$\underline{\underline{L}}^T = \text{differential operator} = \begin{bmatrix} \frac{\partial}{\partial x} & 0 & 0 & \frac{\partial}{\partial y} & 0 & \frac{\partial}{\partial z} \\ 0 & \frac{\partial}{\partial y} & 0 & \frac{\partial}{\partial x} & \frac{\partial}{\partial z} & 0 \\ 0 & 0 & \frac{\partial}{\partial z} & 0 & \frac{\partial}{\partial y} & \frac{\partial}{\partial x} \end{bmatrix}$$

$\underline{\sigma}'$=effective stress vector

$\rho = soil\ density = (1-n)\rho_s + nS\rho_w$

n = soil porosity,

$\rho_s = density\ of\ soil\ particles;$

$S = degree\ of\ saturation; \rho_w = water\ density$

$\underline{g} = vector\ of\ gravity\ acceleration = (0, -g, 0)^T;$

$\underline{\ddot{u}} = (u, v, w)^T$ solid phase acceleration.

– compatibility equations:

$$d\underline{\varepsilon} = \underline{\underline{L}}\, d\underline{u} \tag{a.2}$$

where:
$\underline{\varepsilon}$ = strain vector;
$\underline{u}$ is vector of displacement.

– water dynamic equilibrium:

$$\underline{q} = \underline{\underline{k}}^{int}\left(\nabla u_w + \rho_w \underline{g}\right) \tag{a.3}$$

$$\underline{\underline{k}}^{int} = \begin{bmatrix} \kappa_x/\mu & 0 & 0 \\ 0 & \kappa_y/\mu & 0 \\ 0 & 0 & \kappa_z/\mu \end{bmatrix} \tag{a.4}$$

Table 1
Physical and mechanical parameters assigned to the Conza Dam soils (the Clay_i materials corresponds to different layers of the clay deposit as shown in Fig. 19).

		Clay_1	Clay_2	Clay_3	Clay_4	Clay_5	Filter	Shell	Core
		Foundation clay							
γ_{unsat}	[kN/m^3]	20.10	20.10	20.10	20.10	20.10	18.80	18.20	19.70
c’	[kPa]	55.6	55.60	55.60	55.60	55.60	43.50	8.80	45.50
ϕ’	[°]	19.7	19.70	19.70	19.70	19.70	23.10	44.00	22.60
k_{sat}	[m/s]	2.02E-11	2.20E-11	2.20E-11	2.20E-11	2.20E-11	6.40E-6	4.70E-6	2.90E-11

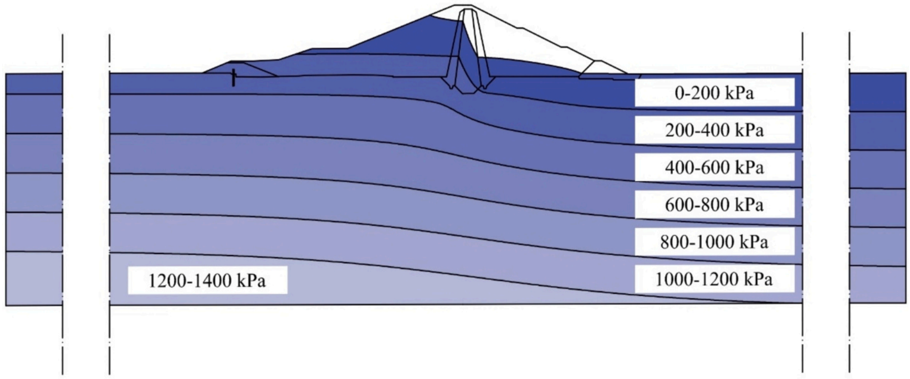

Fig. 18. Steady-state pore water pressure distribution under full impounding of the reservoir.

κ_i = *hydraulic conductivity coefficient along* the *i-direction*

$i = x, y, z$

$k_i = k_{rel}\, k_i^{sat}\; i = x, y, z$

k_i^{sat} = *hydraulic conductivity coefficient at full saturation along* the *i-direction*

$$k_i^{sat} = \rho_w\, g\, \frac{\kappa_{i-intr}}{\mu}\; i = x, y, z \tag{a.5}$$

k_{i-intr}^{t} = *intrinsic hydraulic conductivity along* the *i-direction*

k_{rel} = *ratio between hydraulic conductivity at S and at full saturation*

u_w=*pore water pressure.*

– water continuity equation under dynamic conditions:

$$S\,\underline{m}^T\frac{\partial \underline{\varepsilon}}{\partial t} - n\left(\frac{S}{K_w} - \frac{\partial S}{\partial p_w}\right)\frac{\partial p_w}{\partial t} + \nabla^T\left[\frac{k_{rel}}{\rho_w \underline{g}}\underline{\underline{k}}^{sat}\left(\nabla p_w + \rho_w \underline{g} - \rho_w \underline{\ddot{u}}\right)\right] = 0 \tag{a.6}$$

S = degree of saturation.

The water retention and the hydraulic conductivity functions are expressed according to the Van Genuchten *(1980)* relationships.

The Hardening-Soil-with-small-strain-stiffness (HS-small) constitutive model, initially formulated by Benz *(2006)* and subsequently refined by Brinkgreve et al. *(2007)* and Benz et al. *(2009)*, has been adopted for characterizing the mechanical response of soil zones within the dam system. Rooted in the approach of the original standard version established by Schanz *(1999)* in the original HS-Standard model, the HS-small constitutive model adeptly captures essential macroscopic soil phenomena, including stress-dependent stiffness, overconsolidation, plastic yielding, and dilatancy. These phenomena are thoroughly incorporated within the framework of isotropic-volumetric and isotropic-deviatoric hardening plasticity. The refinements Benz et al. *(2009)* introduced significantly enhance the model predictive capabilities, particularly in the elastic small strain domain. Noteworthy enhancements include incorporating strain-dependent decay of shear stiffness and hysteretic behavior.

The analyses were performed on the discretized geometry displayed in Fig. 19, corresponding to the same analysis domain (Fig. 17) employed in the equivalent linear analysis preceding the Newmark sliding-block simulations.

Based on experimental evidence regarding shell materials, which currently contain high percentages of fine materials and a hydraulic conductivity coefficient of around 10^{-6} m/s, the conventional assumption of shell free-draining behavior under dynamic loads — leading to a predetermined quantification of pore water pressure distribution and enabling a one-phase approach — was excluded. The coupled dynamic approach was subsequently applied to the shells as well.

The simulation of the construction stage entailed activating horizontal layers with an evolution resembling the actual progression of the dam fill level. Initially, the analysis incrementally raised the dam fill level until it reached the embankment level at the Irpinia earthquake in 1980 (approximately 20 m). Subsequently, the analysis processed the seismic event of the Irpinia earthquake. Following this, the analysis resumed the static layered construction until the dam embankment reached completion. The simulation of the static stages ended with applying the boundary conditions consistent with full impounding until attaining steady-state seepage. The analysis of all past stages experienced by the dam (first construction, 1980 earthquake, second construction, impounding) established the initial conditions for stresses and state variables, which served as a basis for subsequent seismic analyses with earthquake scenarios aligned with the limit states required for dam safety assessment.

For the Collapse Limit State (CLS) considered herein, seven spectrum-compatible input signals were used as detailed hereinafter.

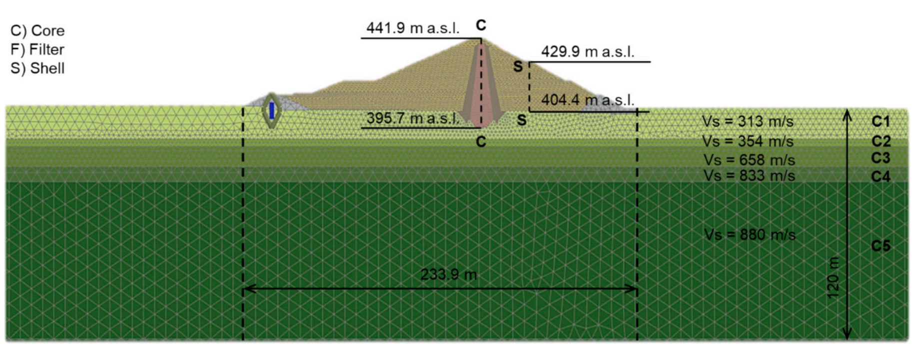

Fig. 19. Discretized geometry of the dam adopted for coupled dynamic analyses.

4. Input signals

In the seismic assessment of dams using performance-based approaches, input signals for each assessment limit state (i.e., Damage Limit State, DLS, or Collapse Limit State, CLS) must be selected from national or international databases, unless simulated using a physics-based deterministic approach. In the first case, the selected signals must ensure spectral compatibility with the target spectrum in both horizontal and vertical directions, while also respecting the seismogenic characteristics of the dam site and limiting the scaling factor of the reference acceleration at the site relative to the recorded value. The Italian technical code *NTC18* (MIT, 2018) defines the reference acceleration at the dam site, PGA_r, as a function of site geographical coordinates and the return period (T_r) of the seismic scenario considered. Together, it provides the reference acceleration spectrum, $S_a(T)_r$, to which the selected seismic signals (i.e., their average acceleration spectrum) over a significant range of periods must conform.

If the Conza dam performance against the Collapse Limit State (CLS) is considered, the return period, T_{CLS}, is equal to 1950 years, and the corresponding horizontal PGA_r on a rock outcrop at the dam site is 0.476 g.

During such a severe earthquake scenario, the dam natural period varies between a minimum (T_{min}) and a maximum (T_{max}), depending on the strain level mobilized in the soil. At the beginning of seismic shaking or during weak-motion stages, the system's dynamics is governed by the small-strain shear stiffness distribution, G_0. In this case, the dam natural period is at its minimum, T_{min}. As the shaking intensity increases, the mobilized shear strain also increases, leading to a decrease in shear stiffness. As a result, the dam natural period tends to increase until it reaches its maximum value, T_{max}.

To define the range of periods for which spectrum compatibility must be ensured, the value of T_{min} should first be determined. Assuming that T_{max} is three times T_{min}, the corresponding T_{max} can then be identified, as will be detailed later.

The natural periods of the Conza Dam embankment in the linear elastic regime (i.e., at small strains) are equal to $T_{0H,e} = 0.422$ s in the horizontal and $T_{0V,e} = 0.281$ s in the vertical direction. These values were obtained by processing the measured values of Vs (G_0) in Fig. 10 through a time-domain dynamic analysis using a white noise as the input signal. The natural periods were then determined by calculating the ratio between the Fourier spectra of the accelerometer signals recorded at the crest and the base of the dam along the embankment centreline axis in the model of Fig. 19**.** It was assumed T_{min} equal to $T_{0V,e} = 0.281$ s and $T_{max} = 3T_{min} \approx 0.9$ s.

Based on seismological studies, the accelerometric records used in the simplified and advanced dynamic analyses were selected from the PEER (Pacific Earthquake Engineering Research center) Ground Motion Database. The spectrum-compatibility was imposed in the identified period interval 0.3 s–0.9 s with a Uniform Hazard Spectrum (UHS) obtained from the seismic hazard analysis, as it is more conservative than the spectrum normally provided by the NTC18. Table 2 shows the most significant parameters of the input signals of the selected events, such as magnitude, epicentral distance, peak acceleration of the two components, mean periods (T_m), Arias Intensity (*AI*) and significant duration ($D_{5\text{–}95}$). The Vs_{30} values associated with the recording stations on rock outcrop ranged between 816 m/s and 1222 m/s. It is worth noting that, in order to achieve spectrum compatibility on the average of the seven selected input signals, recordings from more distant stations were also included in the dataset due to the limited availability of rock outcrop records under near-source conditions.

Before modeling the seismic stages, the accelerometric signals, obtained from rock outcrop recordings, were deconvoluted at a depth of 120 m, where the bottom boundary of the f.e. analysis domain was imposed (Figs. 17 and 19).

5. Analysis results

In reference to the CLS assessment under full impounding, the predictions from the pseudo-dynamic simulations (§3.2) yielded a damage level merely identified with the sliding displacement along the sliding surface S crossing the dam. The predictions from the complete analyses (§3.3) initially focused on the construction stages to achieve the best consistency between computed and observed settlements. The iterative back-analysis procedure required parameter recalibration, which was then used to predict dam response against the CLS earthquake scenario.

5.1. Complete model

The initial set of model parameters was defined based on laboratory and in situ test results. Settlements predicted from the first simulation of the construction stages were used to reproduce the dam construction history, including the 1980 Irpinia earthquake event (the signal recorded at the Calitri station was adopted due to its similar distance and position relative to the 1980 Irpinia fault, as detailed in Dello Russo et al., 2017).

The computed settlements were then compared with the corresponding observed values measured along the core axis (Section 3), which served as a reference for validating the model calibration and assessing its ability to replicate the observed deformation behavior. Only the construction stage was used to re-calibrate parameters, as this exhibits a well-defined deformation patterns under both static and dynamic loading conditions (e.g., the 1980 Irpinia earthquake).

While the computed settlements initially showed good agreement with the observed data, subsequent predictions were refined through slight adjustments to parameters such as E_{50}, E_{oed}, and E_{ur}, thereby improving the data fit (see Table 3). The results (Fig. 20) indicate that the model captures the complex deformation pattern induced by the sequence of dead load and the Irpinia earthquake stage. Specifically, it accounts for changes in the settlement profile, from symmetrical to upwardly distorted shapes, as a result of the seismic deformation induced during construction by the 1980 earthquake.

The seismic assessment under the spectrum-compatible scenario earthquakes according to (MIT, 2018) requires that the most unfavorable operational conditions be assumed as pre-seismic states, corresponding to reservoir impounding inducing steady-state seepage. Full impounding was therefore simulated after dam completion to reproduce a long-term consolidation process leading to the final steady-state condition. The actual sequence of water level fluctuations experienced by

Table 2
Characteristics of the input signals selected on rock outcrop for the CLS scenario.

ID	*Event*	M_w	*Epic.Dist.* (km)	$a_{H,max}$ (g)	$a_{V,max}$ (g)	T_{m_H} (Hz)	T_{m_V} (Hz)	$T_{m\_H}/T_{0H,e,diga}$	$T_{m\_V}/T_{0V,e,diga}$	$AI_{\_H}$ (cm/s)	$AI_{\_V}$ (cm/s)	$D5\text{–}95_{\_H}$ (s)	$D5\text{–}95_{\_H}$ (s)
#680	Whittier Narrows-01	5.99	6.78	0.459	0.537	0.445	0.310	1.05	1.10	147.2	126.9	3.41	6.73
#788	Loma Prieta	6.93	72.90	0.584	0.236	0.682	0.576	1.62	2.05	234.8	60.3	12.13	22.55
#797	Loma Prieta	6.93	74.04	0.549	0.180	0.680	0.782	1.61	2.78	270.0	66.2	14.17	18.09
#804	Loma Prieta	6.93	63.03	0.389	0.138	0.598	0.645	1.42	2.30	244.9	28.9	12.08	15.56
#1011	Northridge-01	6.69	15.11	0.528	0.203	0.315	0.283	0.75	1.01	387.9	32.5	8.71	9.53
#1432	Chi-Chi_Taiwan	7.62	116.64	0.624	0.181	0.968	0.829	2.29	2.95	340.2	112.7	26.42	34.48
#1587	Chi-Chi_Taiwan	7.62	62.11	0.408	0.126	0.563	0.823	1.33	2.93	483.0	83.0	34.13	43.16

Table 3
Physical and mechanical parameters of the HS-small model assigned to dam soils (the Clay_i materials corresponds to different layers of the clay deposit).

		Clay_1	Clay_2	Clay_3	Clay_4	Clay_5	Filter	Shell	Core
		Foundation clay							
γ_{sat}	[kN/m^3]	21.05	21.05	21.05	21.05	21.05	20.00	20.50	20.10
γ_{unsat}	[kN/m^3]	20.10	20.10	20.10	20.10	20.10	18.80	18.20	19.70
e_{init}		0.53	0.53	0.53	0.53	0.53	0.69	0.55	0.55
c'	[kPa]	55.6	55.60	55.60	55.60	55.60	43.50	8.80	45.50
ϕ'	[°]	19.7	19.70	19.70	19.70	19.70	23.10	44.00	22.60
ψ	[°]	0.00	0.00	0.00	0.00	0.00	0.00	0.00	0.00
ν		0.30	0.30	0.30	0.30	0.30	0.30	0.30	0.20
k_0^{nc}		0.66	0.66	0.66	0.66	0.66	0.61	0.31	0.62
E_{50}^{ref}	[MPa]	25.00	25.00	125.00	125.00	187.50	10.63	12.50	6.25
E_{oed}^{ref}	[MPa]	20.00	20.00	100.00	100.00	150.00	8.50	10.00	5.00
E_{ur}^{ref}	[MPa]	75.00	75.00	375.00	375.00	562.50	31.88	37.50	18.75
m		0.50	0.50	0.50	0.50	0.5	0.50	0.50	0.50
G_0^{ref}	[MPa]	210.30	269.00	929.40	1.490E3	1.662E3	154.10	235.30	60.00
$\gamma_{0.7}$		0.15E-3	0.15E-3	0.15E-3	0.15E-3	0.15E-3	0.70E-3	0.35E-3	0.70E-3
k_{sat}	[m/s]	2.02E-11	2.20E-11	2.20E-11	2.20E-11	2.20E-11	6.40E-6	4.70E-6	2.90E-11

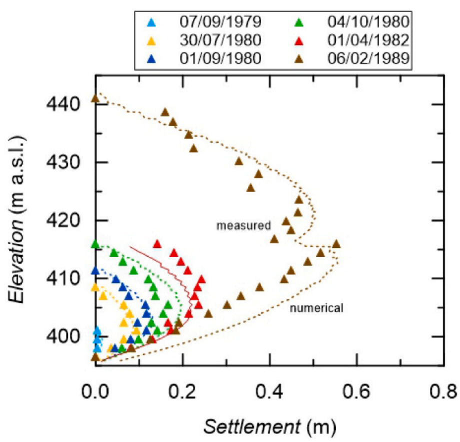

Fig. 20. Measured vs computed settlement profiles in Section 3.

the dam was neglected, and the monitoring data collected over the three decades following the 1980 Irpinia earthquake were not used for further calibration of the model, also considering that the minor deformation patterns observed were considered unsuitable for this purpose. Fig. 21 shows, as an example, the seismic-induced displacements at the dam crest for 4 of the seven pairs (horizontal + vertical) of seismic signals used, specifically the 4 most severe ones (#788, #797, #1432 e #1587), starting from the pre-seismic conditions yielded by the static stage simulation. Vertical ($u_{y(H+V)}$) and horizontal ($u_{x(H+V)}$) displacements were first computed by processing the signals as delivered by seismological study (Case A). In two further analysis sets, vertical displacements were computed assuming the vertical acceleration either reversed ($u_{y(H\text{-}V)}$ for Case B) or eliminated ($u_{y(H)}$ for Case C). It can be noted that in all cases they mostly overlap.

The final permanent settlement cumulates entirely at a time (t*) preceding the end of the shaking stage (t_f) for almost all signals. The maximum permanent settlement computed at the crest is equal to 47 cm for signal #1432. The average settlement on the seven input signals is equal to 27 cm.

Horizontal displacements result in permanent values around zero or downstream directed at the end of the dynamic stage, with a maximum value of 35 cm for signal #1432.

For signals #1432 and #1587, which yielded the most significant permanent settlements, Fig. 22 compares full- against empty-reservoir conditions. It shows how the presence of impounding at a steady state significantly increases permanent settlements by about 50% (47 cm against 31 cm for signal #1432 and 33 cm against 21 cm for signal #1587).

Fig. 23 illustrates typical deformed shapes of the dam body computed at the end of the shaking stage for the input signal # 1432, under both full impounding and empty conditions. Specifically, the pattern appears symmetrical under empty conditions, while it tilts upstream with higher permanent displacements when the reservoir is filled with water.

As initially highlighted in Sica and Pagano *(2009)* and subsequent studies aimed at correlating earthquake intensity measures with dam performance and induced damage levels (Nardo et al., *2024*), the maximum predicted permanent settlements at the dam crest show a strong correlation with the Arias Intensity of the horizontal input acceleration for all processed signals (Fig. 24a), i.e. the vertical displacements generally increase for increasing values of the Arias intensity of the input motion. Five out of the seven signals produce settlement data points closely aligned along a linear trend, while the remaining two generate points significantly below the trend established by the majority. With reference to two combined seismic parameters that can reliably predict the crest settlement proposed by Nardo et al. *(2024)*, namely I_F (referred to as *weighted total power* and given by $I_F = IA{\cdot}T_m$) and ID (referred to as damage intensity, given by $IA{\cdot}T_m/PGV^{0.5}$), it can be noticed that the dispersion related to signals #1011 and #1587 decreases (Figs. 24b and c) and in particular the trend becomes more linear for the I_F parameter (coefficient of determination $R^2 = 0.91$), which takes into account the frequency content of the signal.

According to Sherard *(1986)*, susceptibility to hydraulic fracturing occurs when the ratio R_{HF}, defined as the ratio between the minimum principal total stress, σ_3, and impounding pressure, p_w, reaches unity. Fig. 25 shows the R_{HF} profiles along the core axis, computed at the end of the static stage (pre-seismic conditions) and at the end of the seismic stages. The R_{HF} values, which are quite low in the pre-seismic stage, are further reduced by the seismic deformation pattern, though they always remain above the unity threshold.

Finally, to assess the dam's safety against liquefaction, the evolution of pore pressures was monitored at various control points within the dam body—specifically in the upstream shoulder, the core, and the foundation soil beneath the core—during the seismic loading phase. Along a vertical axis passing through the core, it was observed that control points situated at lower elevations and closer to the dam base tended to develop positive excess pore pressures. Liquefaction safety was evaluated using the liquefaction factor r_u, defined as the ratio between the excess pore pressure at the end of the seismic event and the initial effective vertical stress ($r_u = \Delta u / \sigma'_{vo}$). The r_u values computed at selected control points in the Conza Dam ranged from 0.12 to 0.41, remaining well below the critical threshold ($r_u = 1$) associated with the onset of liquefaction.

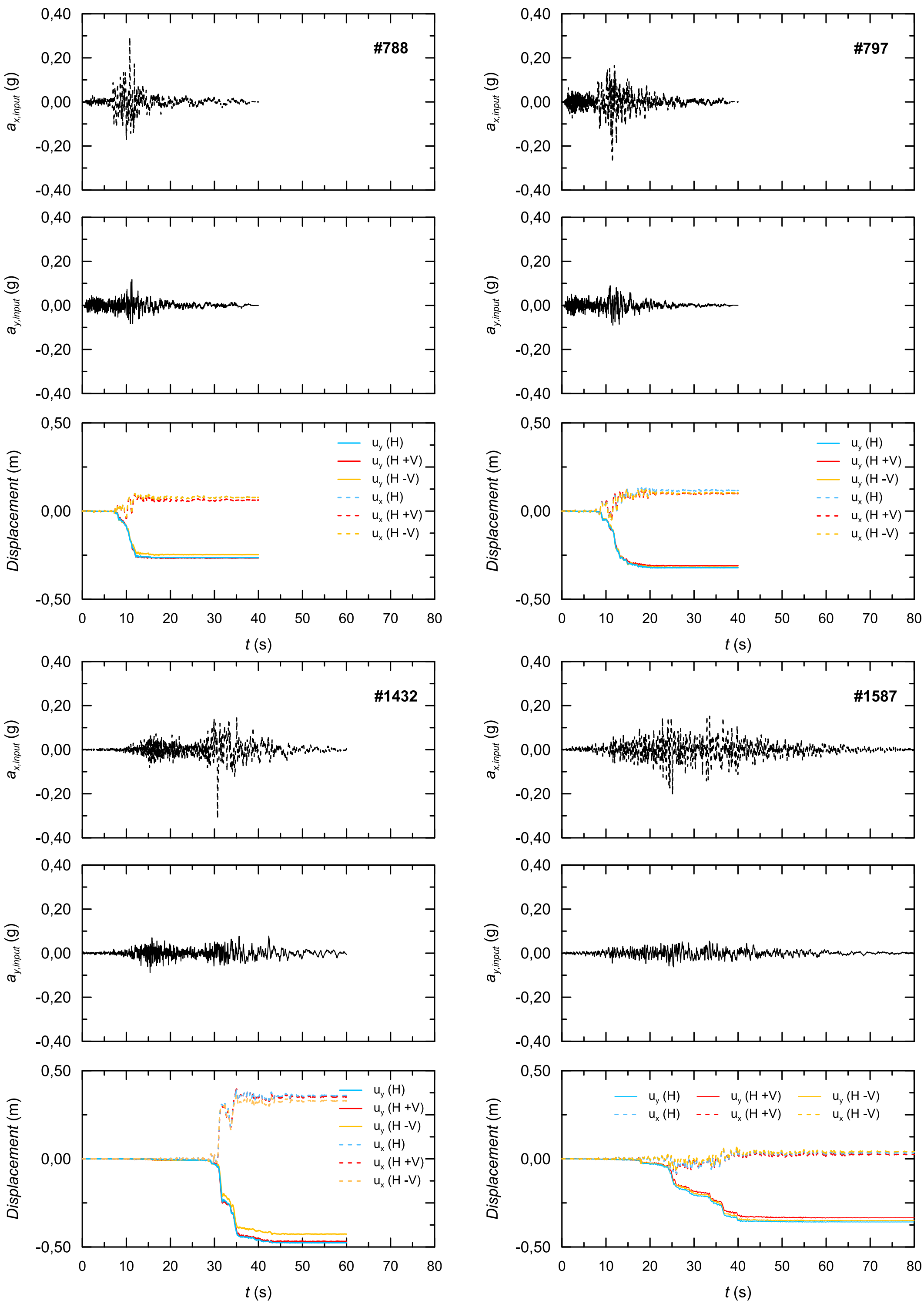

Fig. 21. Input acceleration signals (horizontal, a_x, and vertical, a_y, components) and displacements induced at the dam crest. Specifically, $u_{x(H+V))}$ and $u_{y(H+V))}$ represent the horizontal and vertical displacements computed using both components of the input motion, while $u_{y(H\text{-}V)}$ and $u_{y(H\text{-}V)}$ are the vertical displacements computed by reversing or eliminating the vertical input acceleration, respectively.

5.2. Pseudo-dynamic model

Fig. 26 shows the geometry of four sliding surfaces identified to cross the dam embankment and the shallower foundation soils. In the upstream shell, surface A_m has been selected as it produces the highest sliding displacement across the dam section. Surface B_v, which emerges on the upstream shell surface, crosses the core near its base and emerges downstream the dam toe, has been chosen because it exhibits the greatest displacement among those surfaces that, under full impounding at steady state, cross entirely the core below the zero-pore-water-pressure line, moving downstream. The remaining two surfaces in Fig. 26 represent the counterparts of A_m and B_v in the opposite slope, indicated as A_v and B_m, respectively.

Under full impounding conditions (Fig. 27), the reference analysis

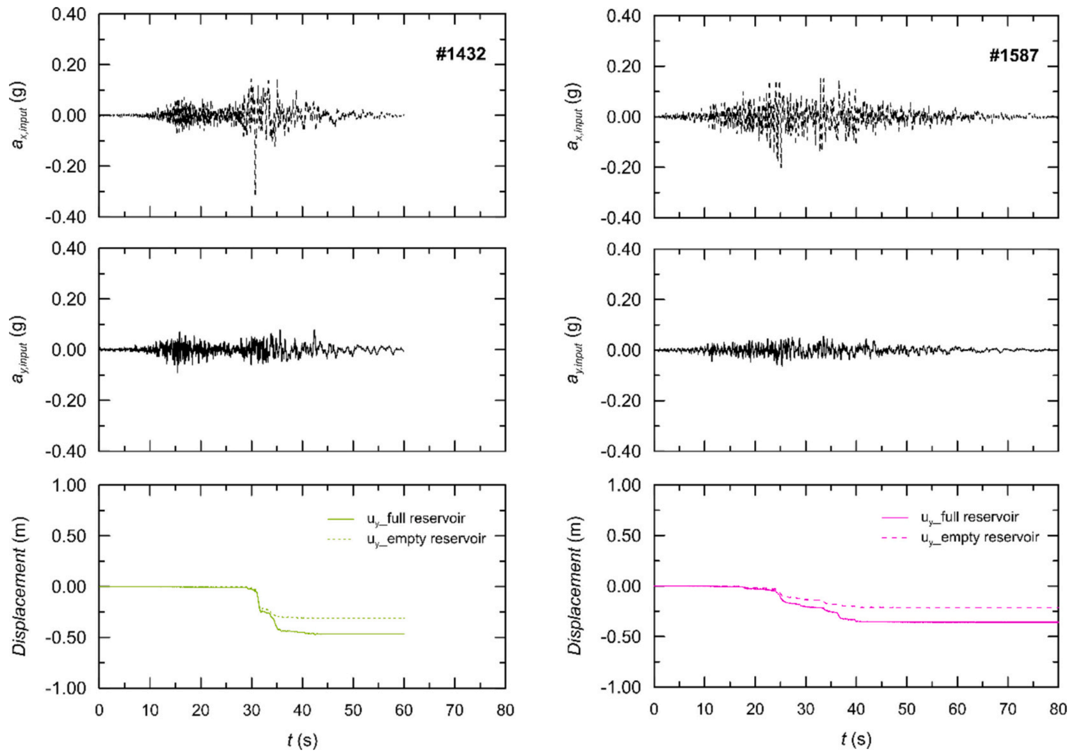

Fig. 22. Input acceleration signals (horizontal, a_x, and vertical, a_y, components) and displacements induced at the dam crest by two pairs of input signals in complete analyses, conducted under both full impounding and empty conditions.

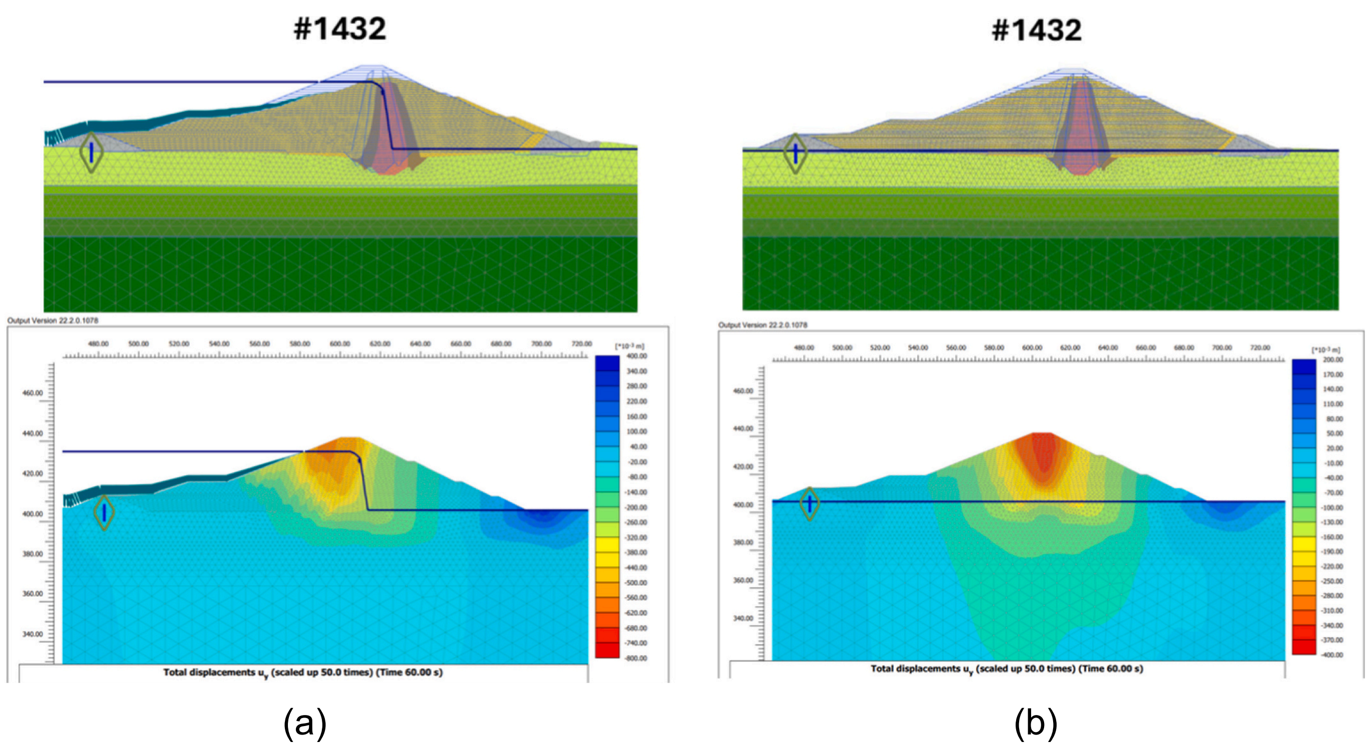

Fig. 23. Deformed shapes and settlement contours induced by signal 1432 under (a) full impounding and (b) empty conditions.

with both input signals (H + V) results in the maximum sliding displacement along B_v, which is 30 cm for signal #688, while the displacement along the upstream counterpart, B_m, is invariably zero for all input signals adopted (Fig. 27a). Further predictions were made by eliminating (case H in Fig. 27b) or reversing (case H-V in Fig. 27c) the vertical acceleration, as done in the complete analyses. In contrast to the reference analysis (H + V), the new analysis sets, H and H-V, yield lower displacements along Bv, suggesting that in the reference analysis, the sign of the vertical accelerations had a stabilizing effect. Accordingly, greater upstream displacements activate for B_m under H and H-V

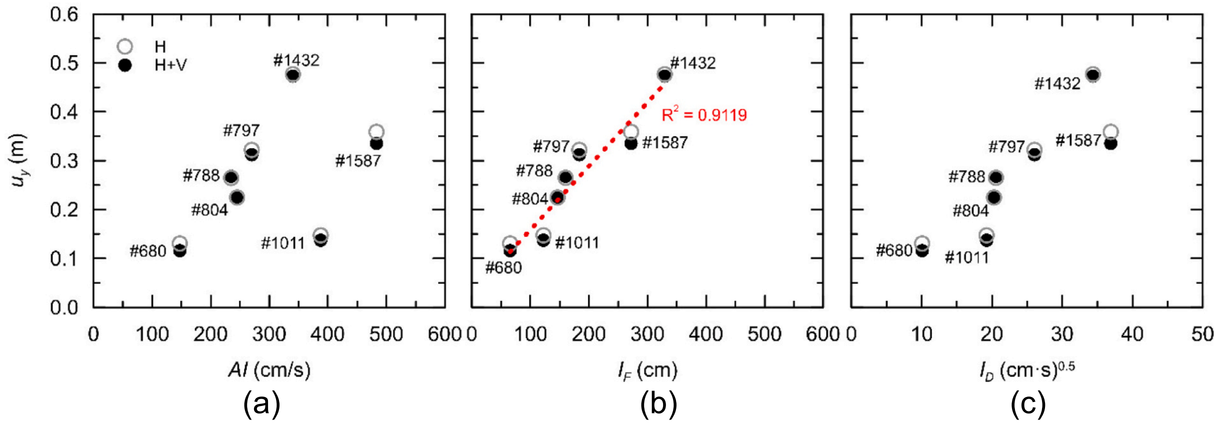

Fig. 24. Permanent crest settlement vs (a) Arias Intensity AI, (b) weighted total power (I_F) and (c) damage intensity (I_D)of the horizontal input acceleration for the seven signals of the CLS scenario, as provided by the complete analysis.

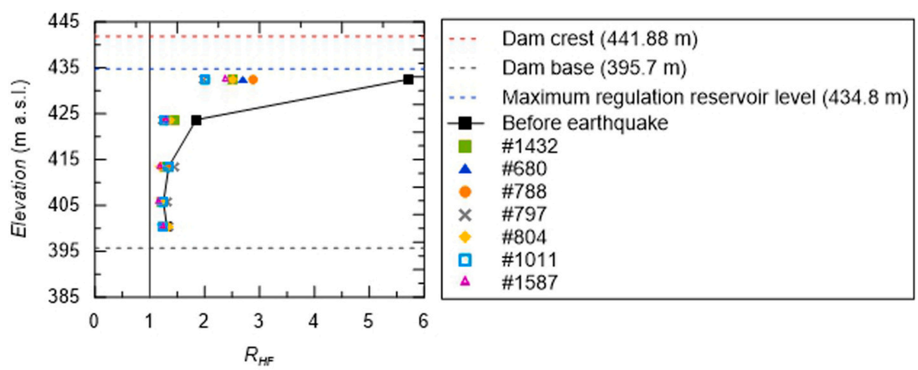

Fig. 25. Local safety factor to hydraulic fracturing, R_{HF}, along the core axis before and at the end of the seismic stage relevant to the seven input signals, as provided by the complete analysis.

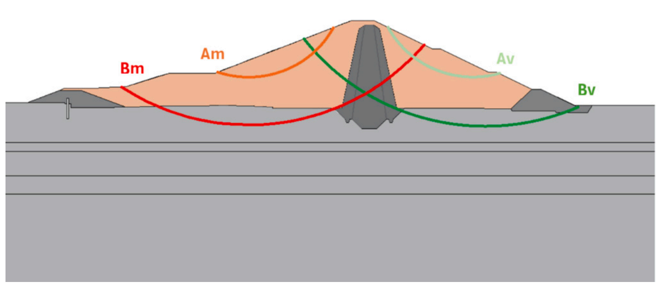

Fig. 26. Most critical sliding surfaces in absolute terms (A_m) and among those crossing the core (B_v), along with their counterparts on the opposite slope. Displacements for all surfaces are presented in the subsequent figures.

scenarios related to the #688 input motion.

In empty conditions (Fig. 28), the reference analyses conducted with the signals (H + V) show that B_v displaces far less than under full impounding (9 against 30 cm). Conversely, B_m experiences a higher displacement (5.5 cm against 0 cm).

6. Discussion

From the outcomes of the performed numerical study, which includes both advanced and simplified dynamic approaches, the following general considerations regarding the seismic performance of the Conza Dam under the Collapse-Limit-State seismic scenario can be drawn.

Referring to the predictions from the complete analysis, the maximum permanent settlements computed at the dam crest are of the same order of magnitude as the maximum sliding displacements estimated by a refined Newmark method along the extended Bv-Bm sliding surfaces that traverse the entire embankment section (Fig. 26). Specifically, the average settlement from the advanced analyses is approximately 20% higher. This difference is consistent with two primary mechanisms contributing to seismic-induced settlements in an earth dam (Sica et al., 2008): diffuse plastic strains and sliding, as opposed to the unique mechanism of sliding considered in the pseudo-dynamic analyses.

Still referring to complete analyses, the relationship between seismic intensity measures and dam performance in terms of crest settlements shows a markedly linear trend if the parameter IF (weighted total power), which takes into account the frequency content of the signal unlike the Arias intensity, is considered.

Under full impounding conditions, deformation in the upstream shell increases significantly. The rise in pore water pressures within this zone reduces the effective stress levels, leading to a corresponding decrease in soil resistance during the seismic stage. The weaker response of the upstream shell is evident from the complete analysis, which reveals a deformational pattern characterized by shell shortening and pronounced core tilting. This behavior is also reflected in the pseudo-dynamic analyses, where sliding displacements are greater for surfaces included in (e.g., A_m) or largely crossing through (e.g., B_v) the upstream shell. In contrast, the downstream shell, characterized by widespread dry conditions, exhibits zero sliding displacements for surfaces included in it (e.g., Av).

In pseudo-dynamic analyses, the vertical acceleration sign affects significantly the size of the displacement for extended surfaces of B_v and B_m types.

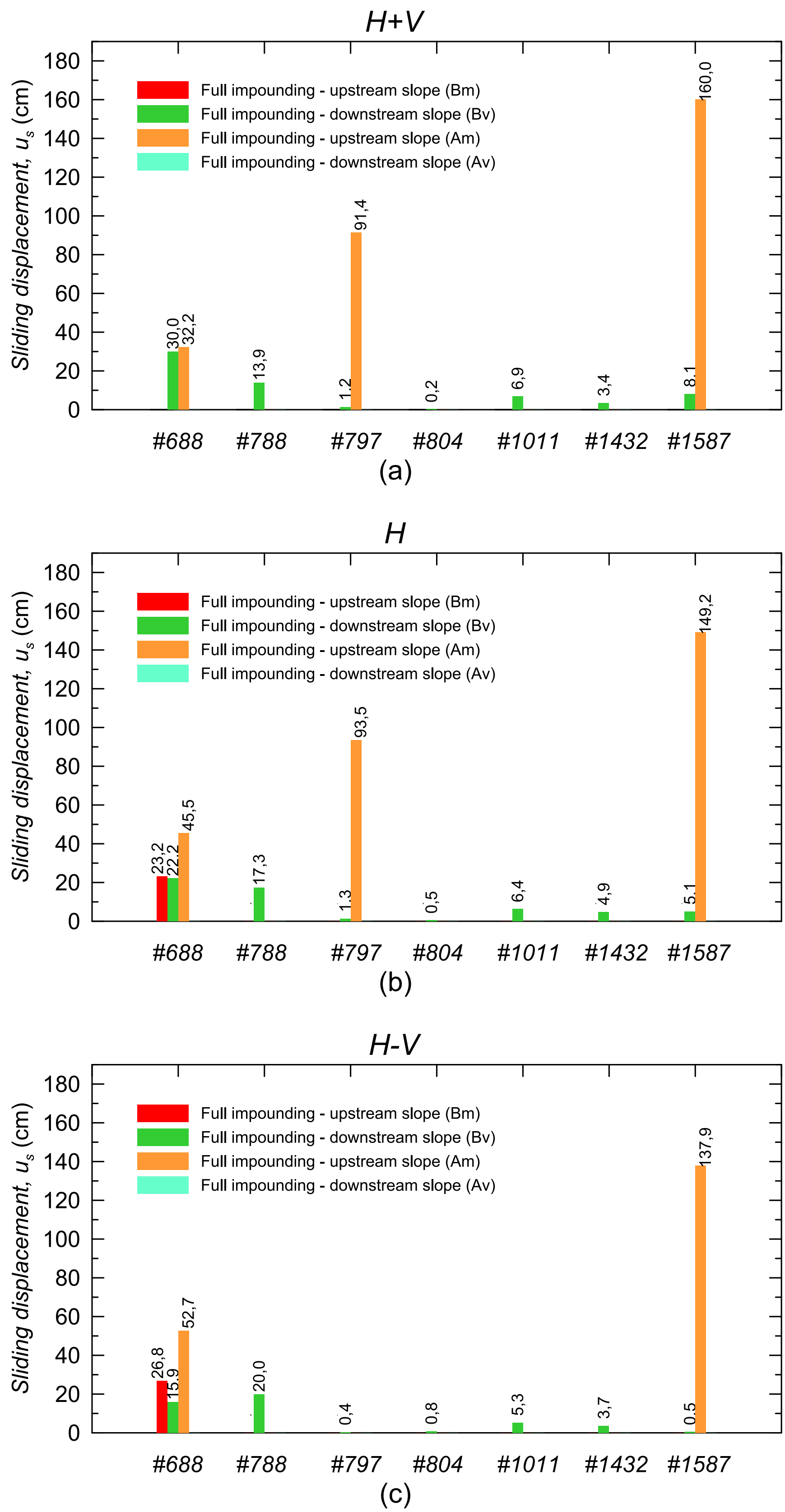

Fig. 27. Sliding displacements computed under full impounding conditions at steady state for the considered sliding surfaces. In (a), displacements induced by the reference seismic scenario (case H + V); in (b) and (c), displacements predicted by eliminating (case H) or reversing (case H-V) the vertical input acceleration, respectively.

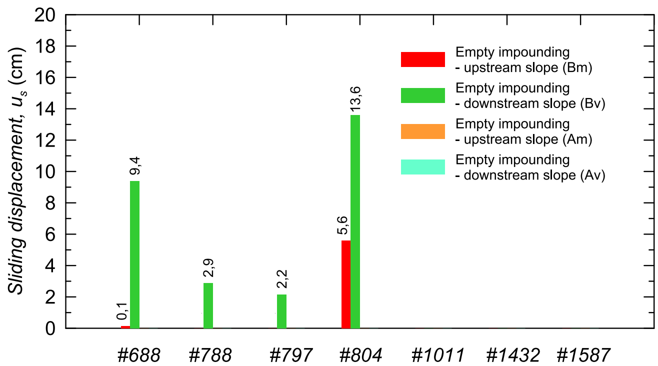

Fig. 28. Sliding displacements computed under empty conditions for the reference seismic scenario (case H + V) and the considered sliding surfaces.

In pseudo-dynamic analyses, the direction of seepage forces within the core and the downstream shell also influences the displacements along the extended surfaces, contributing to B_v displacements being higher in absolute terms compared to those of B_m. Passing from full impounding to empty conditions, B_v displacements decrease primarily due to the significant strength recovery in the upstream shell and, additionally, because of the disappearance of seepage forces that previously promoted downstream movements. Simultaneously, the removal of seepage forces triggers minor displacements along B_m.

Significant A_m-type displacements do not raise safety concerns, as these surfaces are superficial. Conversely, the moderate B_v displacements, from an engineering perspective, represent a core discontinuity that may be susceptible to concentrated leakages during post-seismic stages. Additionally, these discontinuities are likely to persist over time or even expand, as suggested by minimal total stresses computed by complete analyses, which, when compared to the impounding pressure, indicate a susceptibility of the core to hydraulic fracturing. The same B_v displacements, on the other hand, indicate only minor filter dislocations, which have minimal impact on the filter's continuity and do not compromise its functionality.

7. Conclusions

In several applications involving zoned earth dams subjected to seismic loading, the damage level is quantified by predicting the permanent settlement at the embankment crest, without delving into the specific mechanisms that might compromise dam safety, often referring to simplified methods. This practice could be misleading for zoned earth dams, as crest settlements do not always reveal the damage type retrospectively (i.e., damage can increase even with decreasing settlements). Stiffer shells, for instance, settle less but enhance core arching, and consequently, hydraulic fracturing. This demonstrates that settlement is not directly related to the damage level.

In diagnosing the possible damage mechanisms induced by a strong earthquake, the paper redefines the conventional approach hierarchy adopted in the seismic analysis of zoned earth dams, showing that pseudo-dynamic and complete approaches are complementary methods addressing different damage mechanisms, with their combined use providing a more comprehensive and reliable assessment of earthquake-induced deformations.

This concept was illustrated by the case-study of the Conza Dam in Italy, the first documented example of a dam partially raised on a previous seismically deformed embankment. The distinctive seismic-induced settlement pattern, delivered from a thorough interpretation of monitoring data, offered unique evidence for interpreting dam seismic response both empirically and numerically.

The complete approaches mainly quantify core stresses functional to assess susceptibility to hydraulic fracturing, while the pseudo-dynamic ones target the magnitude of dislocation along sliding surfaces that cross the core. Additionally, the paper illustrates how the dam monitoring history, particularly when the dead load and past seismic events produce major deformation, can assist in calibrating various parameters needed in complete analyses. In this perspective, the comparison between previous and recent soil tests further provides insights into potential changes in the physical and mechanical properties of the construction materials over a long operational stage. In overall, the synergistic use of Newmark-type methods and advanced numerical analyses offers a comprehensive understanding of the seismic response of earth dams under real or scenario-based earthquake loading. Drawing on the paradigmatic case of the Conza Dam, this research study provides a valuable reference for guiding seismic assessment procedures of other zoned earth dams located in seismically active regions.

Authors contribution

Mariagrazia Tretola and Lucia Coppola interpreted the results of laboratory and in situ tests for the geotechnical characterization of the dam soils. Mariagrazia Tretola and Lucia Coppola carried out advanced and pseudo-dynamic analyses, respectively.

Stefania Sica and Luca Pagano supervised the overall study through Conceptualization, Supervision, Validation, Writing, Reviewing and Editing.

All authors discussed the results and contributed to the final manuscript.

Ethical approval

All authors approved the submitted manuscript.

Funding

Funding received from the European Union Next-Generation EU (National Recovery and Resilience Plan – NRRP, Mission 4, Component 2, Investment 1.3 – D.D. 1243 2/8/2022, PE0000005). Author Lucia Coppola received research support from the University of Naples Federico II.

Declaration of competing interest

The authors declare that they have no known competing financial interests or personal relationships that could have appeared to influence the work reported in this paper.

Acknowledgments

This study was carried out within the RETURN Extended Partnership and received funding from the European Union Next-Generation EU (National Recovery and Resilience Plan – NRRP, Mission 4, Component 2, Investment 1.3 – D.D. 1243 2/8/2022, PE0000005).

Data availability

The datasets generated during and/or analyzed during the current study are available from the corresponding author on reasonable request.

References

Azadi, A., Esmatkhah Irani, A., Azarafza, M., Hajialilue Bonab, M., Sarand, F.B., Derakhshani, R., 2022. Coupled numerical and analytical stability analysis charts for an earth-fill dam under rapid drawdown conditions. Appl. Sci. 12 (9), 4550.

Beiranvand, B., Komasi, M., 2021. Study of the arching ratio in earth dam by comparing the results of monitoring with numerical analysis (case study: marvak dam). Iran. J. Sci. Technol. Trans. Civ. Eng. 45 (2), 1183–1195.

Benz, T., 2006. Small-Strain Stiffness of Soils and its Numerical Consequences. Stuttgart: Phd Thesis. University of Stuttgart.

Benz, T., Vermeer, P., Schwab, R., 2009. A small-strain overlay model. Int. J. Numer. Anal. Methods Geomech. 33 (1), 25–44.
Bernard, P., Zollo, A., 1989. The Irpinia (Italy) 1980 earthquake: detailed analysis of a complex normal faulting. J. Geophys. Res. Solid Earth 94 (B2), 1631–1647.
Bilotta, E., Pagano, L., Sica, S., 2010. Effect of ground-motion asynchronism on the equivalent acceleration of earth dams. Soil Dyn. Earthq. Eng. 30 (7), 561–579.
Brinkgreve, R.B.J., Kappert, M.H., Bonnier, P.G., 2007. Hysteretic Damping in a Small-Strain Stiffness Model. Proc. of Num. Mod. in Geomech., NUMOG X, Rhodes, pp. 737–742.
Brinkgreve, R.B.J., Kumarswamy, S., Swolfs, W.M., Waterman, D., Chesaru, A., Bonnier, P.G., 2016. PLAXIS 2016. PLAXIS bv, the Netherlands, pp. 1–16.
Casablanca, O., Nardo, A., Biondi, G., Di Filippo, G., Cascone, E., 2022, August. Seismic performance of a zoned earth dam. In: Conference on Performance-Based Design in Earthquake. Geotechnical Engineering. Springer International Publishing, Cham, pp. 1929–1936.
Chen, C., Zhang, L., 2023. Hydro-mechanical behaviour of soil experiencing seepage erosion under cyclic hydraulic gradient. Géotechnique 73 (2), 115–127.
Chen, G., Jin, D., Mao, J., Gao, H., Wang, Z., Jing, L., Li, X., 2014. Seismic damage and behavior analysis of earth dams during the 2008 Wenchuan earthquake, China. Eng. Geol. 180, 99–129.
Choudhury, A., Mishra, S.K., Ghosh, P., 2025. Seismic demand amplification in earth dam by dynamic dam-reservoir interactions (DRI) under near fault pulse type ground motions. Eng. Geol. 344, 107853.
Costigliola, R.M., Mancuso, C., Pagano, L., Silvestri, F., 2022. Prediction of permanent settlements of an upstream faced earth dam. Comput. Geotech. 144, 104594.
Cotecchia, V., Salvemini, A., Ventrella, N.A., 1990. Interpretazione degli abbassamenti territoriali indotti dal terremoti del 23 novembre 1980 e correlazioni con i danni osservati su talune strutture ingegneristiche dell'area epicentrale. Riv. Ital. Geotec. (4/1990).
D.M, 1982. Decreto del Ministro dei LL.PP. 24 marzo 1982 Norme Tecniche per la Progettazione e la Costruzione Delle Dighe di Sbarramento. Gazzetta Ufficiale della Repubblica Italiana n. 212 del 4-8-1982 (in Italian).
Dello Russo, A., Sica, S., Del Gaudio, S., De Matteis, R., Zollo, A., 2017. Near-source effects on the ground motion occurred at the Conza Dam site (Italy) during the 1980 Irpinia earthquake. Bull. Earthq. Eng. 15, 4009–4037.
Deng, Z., Wang, G., Jin, W., Deng, L., Liao, M., Chen, Q., 2025. Suffusion characteristics of a heterogeneous dam foundation with a cut-off wall of stochastic defects. Eng. Geol. 344, 107829.
DGD, 2019. Circolare della D.G. Dighe 3 luglio 2019. n. 16790 Verifiche sismiche delle grandi dighe, degli scarichi e delle opere complementari e accessorie - istruzioni per l'applicazione della normativa tecnica (in Italian).
Gao, Y., Wang, L., Sun, S., Zhang, Y., Pan, J., Gao, Y., 2023. Seismic performance of small and medium-sized homogeneous earthen dams considering valley site effects in large-scale shaking table tests. Eng. Geol. 318, 107098.
GeoStudio, 2003. Licensed to Università di Napoli Federico II. Geo-Slope International Ltd., Calgary, Canada.
ICOLD, 2002. Earthquake design and evaluation of structures appurtenant to dams, Bulletin 123, Committeeon Seismic Aspects of Dam Design. ICOLD, Paris.
Marsal, R.J., Sandoval, R., Hiriart, F., 1950. Curvas deformación-tiempo en las arcillas del Valle de México. Ing. Civ. 2 (V), VII–17. Colegio de Ingenieros Civiles de Mexico.
MIT, Ministero Infrastrutture e Trasporti. NTC18, 2018. Aggiornamento delle Norme Tecniche per le Costruzioni (Decreto Ministeriale 17-01-2018) e Istruzioni per l'applicazione delle NTC2018. Gazzetta ufficiale n. 35 dell'11-02-2019 (In Italian).
MIT, Ministero Infrastrutture e Trasporti. NTD14, 2014. Norme Tecniche per la Progettazione e la Costruzione degli Sbarramenti di Ritenuta (dighe e traverse). Decreto 26/06/2014. Gazzetta Ufficiale Serie Gen, p. 156 del 08/07/2014 (in Italian).
Nardo, A., Biondi, G., Casablanca, O., Di Filippo, G., Cascone, E., 2024. Seismic intensity measures and predictive equations for the evaluation of earthquake—induced crest settlements of earth dams. Earthq. Eng. Struct. Dyn. 53 (9), 2680–2709.
Newmark, N.M., 1965. Effects of earthquakes on dams and embankments. Geotechnique 15 (2), 139–160.
Pagano, L., Sica, S., Desideri, A., 2006. Representativeness of measurements in the interpretation of earth dam behaviour. Can. Geotech. J. 43 (1), 87–99.
Pagano, L., Mancuso, C., Sica s., 2008. Prove in sito sulla diga del Camastra: tecniche sperimentali e risultati. Riv. Ital. Geotec. XLII (3), 11–28.
Pagano, L., Russo, C., Sica, S., Costigliola, R.M., 2019. Earth dams: damage mechanisms and limit states in seismic conditions. In: Earthquake Geotechnical Engineering for Protection and Development of Environment and Constructions. CRC Press, pp. 600–616.
Pagano, L., Tretola, M., Sica, S., 2024. A parametric study to characterize the impact of soil water retention curves on the seismic response of earth dams. Riv. Ital. Geotec. 4, 65.
Papadimitriou, A.G., Bouckovalas, G.D., Andrianopoulos, K.I., 2014. Methodology for estimating seismic coefficients for performance-based design of earthdams and tall embankments. Soil Dyn. Earthq. Eng. 56, 57–73.
Pereira, S., Magalhaes, F., Gomes, J.P., Cunha, A., Lemos, J.V., 2018. Dynamic monitoring of a concrete arch dam during the first filling of the reservoir. Eng. Struct. 174, 548–560.
Schanz, M., 1999. A boundary element formulation in time domain for viscoelastic solids. Commun. Numer. Methods Eng. 15 (11), 799–809.
Sherard, J.L., 1986. Hydraulic fracturing in embankment dams. J. Geotech. Eng. 112 (10), 905–927.
Sica, S., Dello Russo, A., 2021. Seismic response of large earth dams in near-source areas. Comput. Geotech. 132, 103807.
Sica, S., Pagano, L., 2009. Performance-based analysis of earth dams: procedures and application to a sample case. Soils Found. 49 (6), 921–939.
Sica, S., Pagano, L., Modaressi, A., 2008. Influence of past loading history on the seismic response of earth dams. Comput. Geotech. 35 (1), 61–85.
Van Genuchten, M.T., 1980. A closed-form equation for predicting the hydraulic conductivity of unsaturated soils. Soil Sci. Soc. Am. J. 44 (5), 892–898.
Vucetic, M., Dobry, R., 1991. Effect of soil plasticity on cyclic response. J. Geotech. Eng. 117 (1), 89–107.
Wang, D., Zhou, Y., Pei, X., Ouyang, C., Du, J., Scaringi, G., 2021. Dam-break dynamics at Huohua Lake following the 2017 Mw 6.5 Jiuzhaigou earthquake in Sichuan, China. Eng. Geol. 289, 106145.